© 2016. Published by The Company of Biologists Ltd | Journal of Cell Science (2016) 129, 1697-1710 doi:10.1242/jcs.188409

RESEARCH ARTICLE

Influenza A virus ribonucleoproteins modulate host recycling by competing with Rab11 effectors

Sílvia Vale-Costa[1], Marta Alenquer[1], Ana Laura Sousa[2], Bárbara Kellen[1], José Ramalho[3], Erin M. Tranfield[2] and Maria João Amorim[1,*]

ABSTRACT

Influenza A virus assembly is an unclear process, whereby individual virion components form an infectious particle. The segmented nature of the influenza A genome imposes a problem to assembly because it requires packaging of eight distinct RNA particles (vRNPs). It also allows genome mixing from distinct parental strains, events associated with influenza pandemic outbreaks. It is important to public health to understand how segmented genomes assemble, a process that is dependent on the transport of components to assembly sites. Previously, it has been shown that vRNPs are carried by recycling endosome vesicles, resulting in a change of Rab11 distribution. Here, we describe that vRNP binding to recycling endosomes impairs recycling endosome function, by competing for Rab11 binding with family-interacting proteins, and that there is a causal relationship between Rab11 ability to recruit family-interacting proteins and Rab11 redistribution. This competition reduces recycling sorting at an unclear step, resulting in clustering of single- and double-membraned vesicles. These morphological changes in Rab11 membranes are indicative of alterations in protein and lipid homeostasis during infection. Vesicular clustering creates hotspots of the vRNPs that need to interact to form an infectious particle.

KEY WORDS: Correlative light and electron microscopy, Rab11, Influenza A virus assembly, Membrane trafficking, Recycling endosome

INTRODUCTION

Influenza A virus (IAV) causes yearly epidemics and recurrent pandemics of severe outcomes and increased mortality. The virus has a negative-sense segmented RNA genome that encodes up to 18 identified polypeptides (Yamayoshi et al., 2015). Each segment is arranged as a viral ribonucleoprotein (vRNP) by forming a complex with one copy of the viral RNA polymerase and several copies of nucleoprotein. Upon entrance, vRNPs are transported to the nucleus for replication. Newly synthesized vRNPs are then exported to the cytoplasm and transported to the apical plasma membrane where virion assembly, budding and release occurs (Hutchinson and Fodor, 2013). Virion assembly involves selective packaging of RNA segments into an M1-coated cavity that is delimited by plasma membrane, where the transmembrane proteins hemagglutinin (HA), neuraminidase and M2 are embedded. The selection of the eight-segment core is important for viral assembly because the majority of virions incorporate no more than eight segments (Bergmann and Muster, 1995; McGeoch et al., 1976; Chou et al., 2012; Noda et al., 2006). Formation of the core is thought to occur through a hierarchical network of RNA–RNA interactions among segments (Fujii et al., 2005; Gavazzi et al., 2013; Gog et al., 2007). Genomic segmentation permits emergence of reassortant viruses through the mixing of distinct parental genomes during co-infection. Reassortment is a fundamental mechanism for interspecies transmission because progeny viruses can overcome adaptive host barriers faster by acquiring beneficial alleles from circulating viruses. Consistently, reassortants have been associated with excess mortality in pandemics (Morens et al., 2009; Herfst et al., 2014). It is thus of interest to human health to explain the mechanisms underlying selection of the eight-segment vRNPs to form an infectious virion, to which trafficking of vRNPs to the surface contribute.

Recently, it has been shown that IAV vRNPs attach to Rab11 vesicles after nuclear export, and depletion of the two isoforms of Rab11 (Rab11a and Rab11b, henceforward Rab11 refers to both isoforms) impacts negatively on viral production (Amorim et al., 2011; Avilov et al., 2012b; Eisfeld et al., 2011; Momose et al., 2011). Rab11 is the master regulator of the recycling endosome, described as a web of tubulovesicular membranes (Mobius et al., 2003), that deliver endocytosed proteins and lipids, as well as material segregated from the trans-Golgi network, to the surface. Given their function, it has been postulated that the recycling endosome transports vRNPs to the surface using the microtubule network (Amorim et al., 2011; Momose et al., 2011). Later, it was shown that several vRNPs colocalize in a Rab11-dependent manner in cytosolic puncta that increase in size with infection, which led to the proposal that assembly of the 8-segment core occurs en route to the surface (Chou et al., 2013; Lakdawala et al., 2014). Collectively, these data place Rab11a as being central for viral assembly, with many unresolved questions.

First, the binding partners linking vRNPs and Rab11a-positive tubulovesicular membranes have not been unequivocally identified. Two studies have implicated the PB2 subunit of the viral polymerase in binding (Amorim et al., 2011; Momose et al., 2011), although it is unclear whether the interaction is indirect. Second, the morphology and cellular spatial arrangements of Rab11a vesicles carrying vRNPs is undefined at an ultrastructural level and could reveal rearrangements on Rab11 membranes during infection, providing clues as to their role. So far, these studies have failed because of the lack of (1) ultrastructural resolution in methods employing fluorescence microscopy, which are able to distinguish individual vRNPs but not cellular membranes (Henriques et al., 2011) and (2) efficient processes to mark vRNPs for electron microscopy analyses. How the binding of vRNPs to Rab11 affects the sorting of Rab11 tubulovesicles (and the processes they control) has also not been addressed.

[1]Cell Biology of Viral Infection Lab, Instituto Gulbenkian de Ciência, Rua da Quinta Grande, 6, Oeiras 2780-156, Portugal. [2]Electron Microscopy Facility, Instituto Gulbenkian de Ciência, Rua da Quinta Grande, 6, Oeiras 2780-156, Portugal. [3]Centro de Estudos de Doenças Crónicas (CEDOC), Faculdade de Ciências Médicas, Universidade Nova de Lisboa, Lisboa, Portugal.

*Author for correspondence (mjamorim@igc.gulbenkian.pt)

Received 22 February 2016; Accepted 29 February 2016

Journal of Cell Science

Journal of Cell Science (2016) 129, 1697-1710 doi:10.1242/jcs.188409

In normal circumstances, the GTPase Rab11a is activated upon GDP–GTP exchange (Xiong et al., 2012), binding several effectors – including molecular motors – that drag vesicles along cytoskeleton tracks (Kelly et al., 2012). Interestingly, this transport is facilitated by Rab11-family-interacting proteins (FIPs) that work as adaptors or increase the affinity of motors for membranes (Welz et al., 2014). Their depletion negatively impacts on recycling efficiency (Schonteich et al., 2008). When vesicles reach the acceptor membrane, Rab11 recruits tethers and other proteins that are responsible for vesicular fusion (Sato et al., 2008; Zhang et al., 2004).

Here, we addressed at the molecular level the consequences of binding of vRNPs to the recycling compartment. We show that binding of vRNP to Rab11 vesicles outcompeted the ability of Rab11 to bind to its effector FIPs, resulting in impaired recycling. We also show that there is a causal relationship between Rab11-FIP recruitment and the distribution of Rab11. Using correlative light and electron microscopy (CLEM), we observed clustering of vesicles that were positive for Rab11a and vRNPs, creating vRNP hotspots scattered in the cytosol. These vesicles were heterogeneous, and comprised single and double membranes, indicating an alteration in vesicular morphology and lipid homeostasis. We believe that the observations described here help to further elucidate IAV assembly and reassortment at a molecular level.

RESULTS

IAV infection induces alterations in Rab11a distribution, leading to reduced recycling efficiency

Previous reports have shown that the recycling endosome suffers alterations in distribution during IAV infection, which have not been characterized at ultrastructural or molecular levels. In fact, Rab11 distribution changes with infection from discrete puncta to enlarged structures (Amorim et al., 2011; Chou et al., 2013; Eisfeld et al., 2011). This conclusion originated from confocal microscopy analyses from four independent studies, using different systems, including a mini-replicon system that was devoid of segments 4 and 6 (Amorim et al., 2011), and infection with wild-type viruses (Avilov et al., 2012a; Eisfeld et al., 2011; Momose et al., 2011). To determine the viral factors that provoke changes in the recycling compartment, we quantified the changes in Rab11 distribution during infection (Fig. 1A). Using confocal images, we measured Rab11 vesicular areas in infected and control cells. We then assigned them into intervals according to size (Fig. 1B and C): small vesicles measured up to 0.15 μm^2, medium vesicles ranged between 0.15 and 0.30 μm^2 and large vesicles were bigger than 0.30 μm^2 (examples in Fig. 1B). The smallest interval is consistent with the published areas for Rab11 vesicles in uninfected cells (Mobius et al., 2003), and includes 90.7% of the population analyzed. The intermediate class represents up to a twofold increase in area, which in uninfected cells corresponds to 8.4% of vesicles, and the upper interval includes vesicles bigger than 0.3 μm^2, corresponding to the exceptional 0.9% of the population in control. Data from three independent experiments showed that the frequency of small vesicles decreased from 90.7±3.5% to 39.9±4.7% (mean±s.e.m.) throughout infection. Conversely, the frequency distribution of larger vesicles augmented from 8.4±3.1% to 30.1±1.1% (medium size) and 0.9±0.5% to 29.0±4.8% (large vesicles), becoming statistically significant from 16 h post infection onwards (Fig. 1C). To confirm that these changes were induced by vRNPs and not by other viral proteins, we quantified the increase in the size of Rab11 vesicles over the course of infection after inhibiting the nuclear export of vRNPs using leptomycin B (LMB), as previously described (Elton et al., 2001; Ma et al., 2001). If vRNPs were responsible for alterations in the recycling endosome without interference of any other viral factor, then inhibiting nuclear export of vRNPs during infection would not affect its morphology. In the presence of LMB, vRNPs were greatly retained in the nucleus (Elton et al., 2001) (Fig. 2B), compared with their cytosolic location from 8 h post infection onwards in the control (Fig. 2A). vRNP nuclear retention resulted in the maintenance of Rab11 vesicular areas in the small interval until 24 h post infection, although a modest increase of 11% in the intermediate class was observed (compare Fig. 2D and E). In previous reports, LMB addition to cells has resulted in a reduction in virus titers of 90 to 95%, indicating that sufficient vRNPs can still reach the plasma membrane in order to form virions (Elton et al., 2001; Ma et al., 2001). This incomplete blockade in vRNP export might justify some degree of alteration in the recycling endosome. To completely exclude a role of other viral proteins in this alteration, we quantified the size of Rab11 vesicles in cells that had been transfected individually with GFP-tagged NEP/NS2, NS1, M1 and M2 (Fig. 2C and F). None of these proteins caused a significant increase in Rab11 vesicles, with a minor variation in the middle interval of 12.1, 8.5, 13.8 and 3.3%, respectively, in relation to the control (Fig. 2F). Because alterations in recycling endosomes have been observed using the mini-replicon system, devoid of HA and neuraminidase (Amorim et al., 2011), we excluded these viral proteins from the analysis. This set of experiments confirmed that vRNPs are responsible for changes in Rab11 distribution by performing confocal microscopy analysis.

The increase in Rab11a puncta that was induced by infection suggested that the recycling capacity of infected cells was impaired. To test this hypothesis, we quantified, in confocal snapshots, the uptake and recycling of fluorescently-labeled transferrin, a well-known cargo of recycling endosomes (Lakadamyali et al., 2006). For this, we quantified the intensity of transferrin upon 10 min of uptake and 10 min of recycling. We observed that both the uptake and recycling capacity diminished during infection, and that overall recycling efficiency was reduced by 40±5% at 8 h post infection and by 77±9% at 12 h post infection (Fig. 1D). Our results, therefore, show that IAV infection reduces the recycling efficiency of the infected cell.

FIPs, when overexpressed, outcompete vRNPs for Rab11a binding

Our data indicate that Rab11 redistributes upon vRNP binding and impairs recycling endosome sorting efficiency by an unknown mechanism. Sorting impairment could be attributed to reduced recruitment of Rab11a effectors. To test this hypothesis, we inquired whether the extensively characterized Rab11 effectors, FIPs, bound to Rab11a efficiently during infection. FIP competition with vRNPs for Rab11 binding has been previously explored by Momose et al. (2011), but the results are not unequivocal. In this work, overexpressing the homologous Rab-binding domain (RBD) of FIPs impeded vRNPs from displaying the enlarged puncta that are characteristic of infection. Also, overexpression of individual FIPs that lacked the RBD preserved the vRNP punctate distribution. Direct binding of vRNPs to Rab11 could explain these results, but one cannot exclude other scenarios, particularly in the absence of *in vitro* confirmation. For example, vRNPs could bind to Rab11 through a domain in FIPs that is distinct from the RBD. In agreement, different FIPs share functional domains, with type-I FIPs (FIP1B, FIP1C, FIP2 and FIP5) exhibiting C2 domains, and type-II FIPs (FIP3 and FIP4) EF hand domains, and these could

Journal of Cell Science (2016) 129, 1697-1710 doi:10.1242/jcs.188409

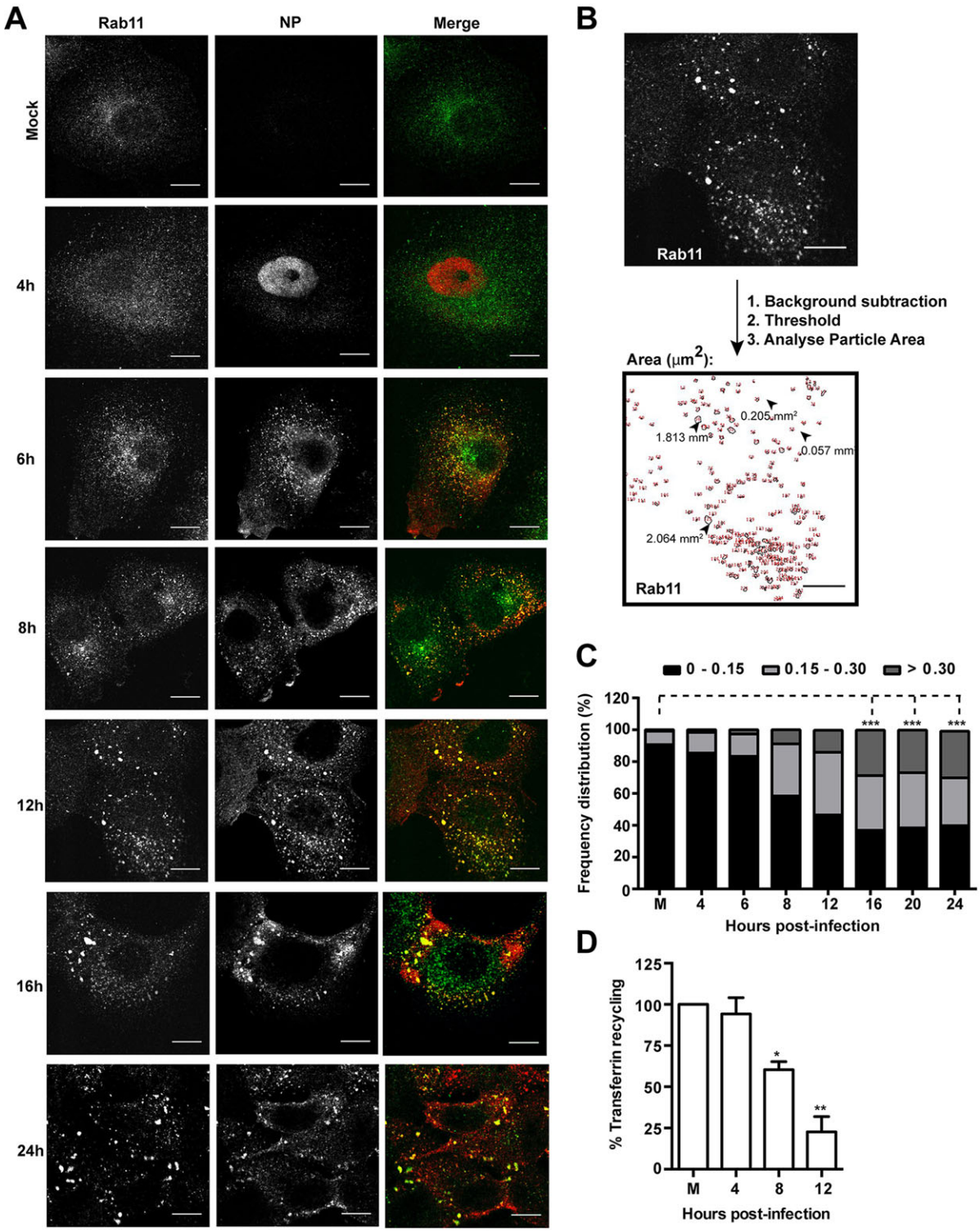

Fig. 1. IAV infection induces alterations in the Rab11a distribution, leading to reduced recycling efficiency. A549 cells were infected or mock-infected with PR8 at a multiplicity of infection (MOI) of 3. (A) At the indicated time points, cells were fixed and processed for immunofluorescence staining of endogenous Rab11 and viral nucleoprotein protein (NP; as proxy for vRNPs). Scale bars: 10 µm. (B) The area of Rab11 vesicles in each cell was quantified using ImageJ software (NIH), as briefly exemplified. Firstly, each image was converted to 8-bit color and then a 'background subtraction' of 20 pixels was applied, followed by a 'threshold' adjustment of 14 (lower level) – 255 (upper level). Finally, the 'analyze particle' function was used to quantify the area (in μm^2) of each vesicle inside selected cells. Scale bars: 10 µm. (C) The frequency distribution of three size categories in the areas (in μm^2) of Rab11 vesicles (small, medium and large) was plotted over the course of infection. The graph shows a pool of data from three independent experiments. An average of 20 cells, per experiment, was analyzed per time point. Statistical analysis of data was performed using non-parametric two-way ANOVA test, followed by Tukey multiple comparisons test (***P<0.001). Note that the statistics depicted only include the larger group compared to mock (M). (D) At the indicated time points, transferrin recycling efficiency (%±s.e.m.) was plotted as the difference in signal intensity of confocal images detected in cells after transferrin uptake and recycling. Statistical analysis of data was performed using one-way ANOVA test, followed by Dunnett's multiple comparisons test (*P<0.05; **P<0.01). The graph shows a pool of data from two independent experiments. An average of 100 cells were analyzed per condition per experiment.

Journal of Cell Science (2016) 129, 1697-1710 doi:10.1242/jcs.188409

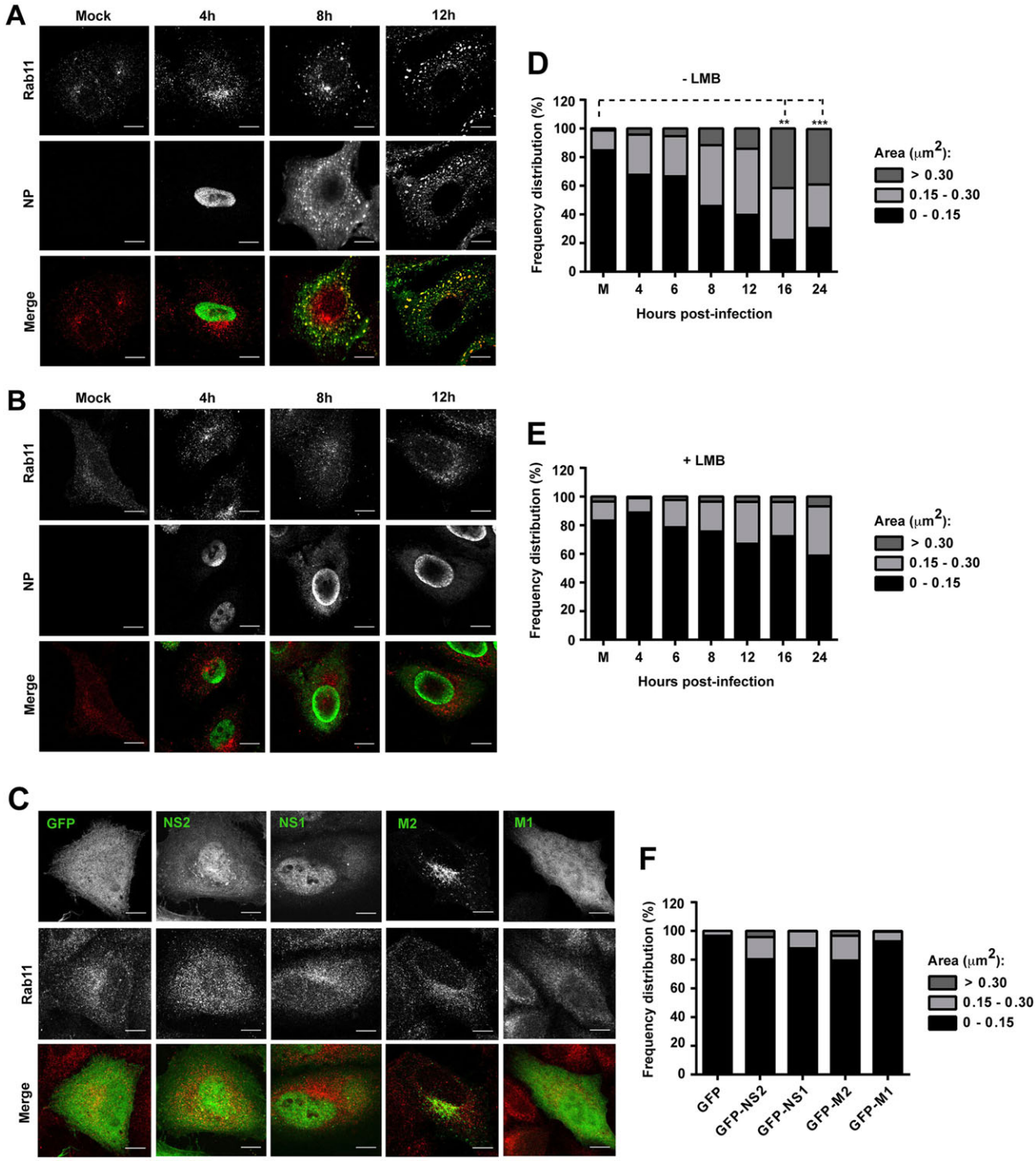

Fig. 2. Nuclear export of vRNPs, but not other viral factors, is required for Rab11a-vesicle size increase. (A,B) A549 cells were infected or mock-infected with PR8 at a MOI 3. At 3.5 h post infection, cells were treated (B) or not (A) with 10 nM of LMB. At the indicated time points, cells were fixed and processed for immunofluorescence staining of endogenous Rab11 and viral nucleoprotein (NP; as a proxy for vRNPs). (C) HeLa cells were transfected with GFP or GFP-tagged viral proteins (NS2, NS1, M2 and M1) for 14 h. After this period, cells were fixed and processed for immunofluorescence staining of Rab11. (D–F) The frequency distribution of vesicles within the three size categories in the areas (in μm^2) of Rab11 vesicles (small, medium and large) was plotted. Statistical analysis of data was performed using a non-parametric Kruskal–Wallis test, followed by Dunn's multiple comparisons test (**P<0.01; ***P<0.001). An average of 30 cells were analyzed per condition. Graph compares conditions within the same experiment, and statistical analysis compares only the larger interval of all samples to the mock (D,E) or GFP condition (F). M, mock. Scale bars: 10 µm.

substitute for non-functional or depleted FIPs (Baetz and Goldenring, 2013). Also, FIP binding to Rab11 could be essential to grant access of FIPs to vRNPs (Wei et al., 2009). This means that without the RBD, FIPs would fail to bind vRNPs. To understand the ability of Rab11a to recruit individual proteins, we generated an artificial targeting system to anchor Rab11a to the mitochondria and analyze the relocation of individual effectors (Fig. 3A; Fig. S1). This strategy was attractive because it can be used to investigate

Journal of Cell Science (2016) 129, 1697-1710 doi:10.1242/jcs.188409

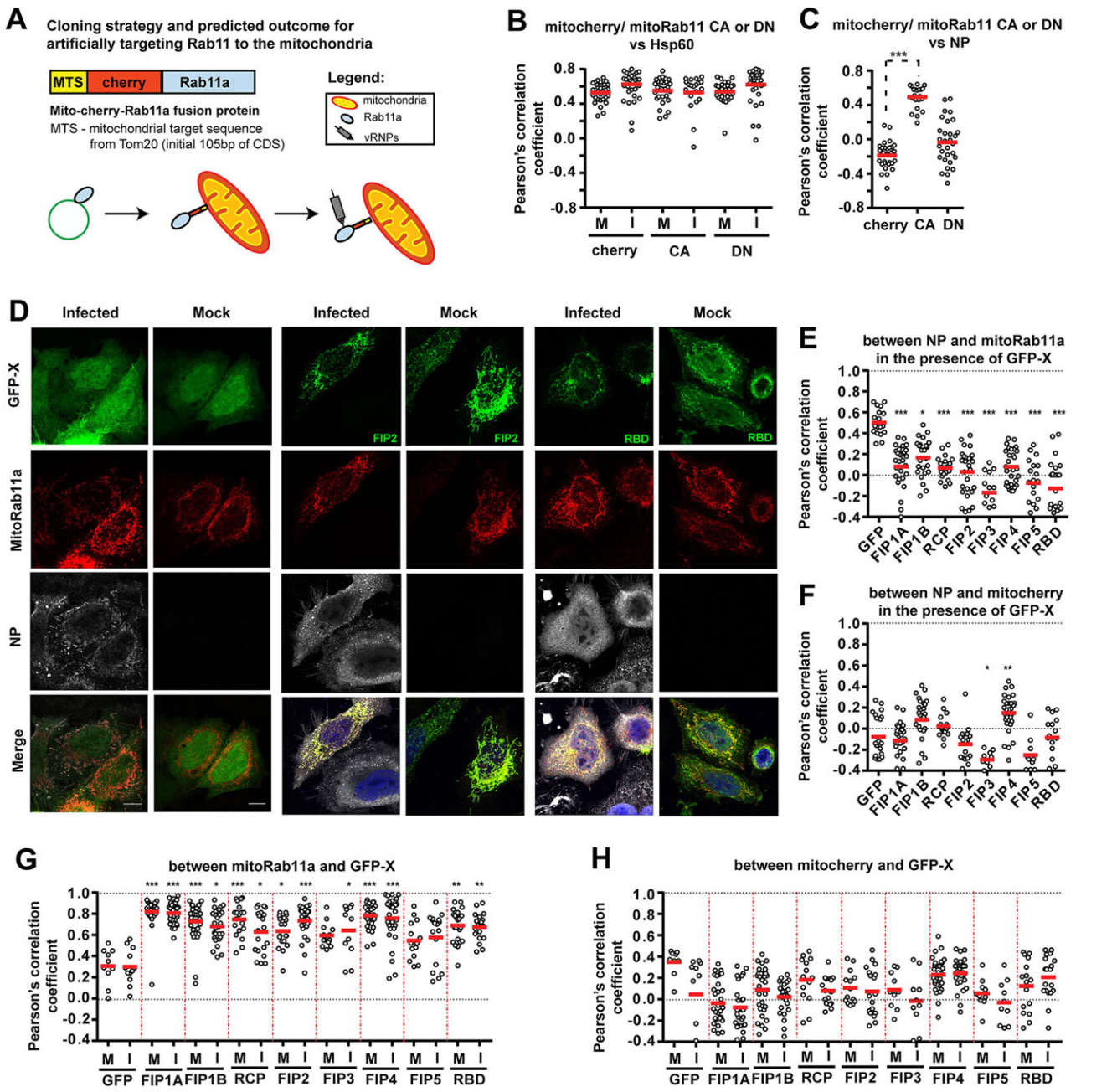

Fig. 3. FIPs outcompete vRNP binding to Rab11a that has been artificially anchored at the mitochondria. (A) Cloning strategy to artificially target Rab11a to the mitochondria for vRNP recruitment to this organelle. (B,C) Constitutively active (CA) and dominant-negative (DN) forms of Rab11a protein tagged with Cherry at the N-terminus, or Cherry only, were targeted to the mitochondria by fusion with the MTS of Tom20 (mitoRab11aCA and mitoRab11 DN, and mitoCherry). HeLa cells were transfected with these three plasmids individually and infected with PR8 at MOI 20. At 14 h post infection, cells were fixed and processed for immunofluorescence staining of Hsp60 and/or viral nucleoprotein (Fig. S1). (B) Colocalization between Hsp60 and mitoCherry, mitoRab11a CA or mitoRab11a DN, in mock-infected ('M') or infected ('I') cells, was plotted using the Pearson's correlation coefficient calculated using ImageJ software (NIH). (C) The colocalization between nucleoprotein and mitoCherry, mitoRab11aCA or mitoRab11aDN in infected cells was plotted as described in B. (D) HeLa cells were co-transfected with mitoRab11aCA and either GFP alone or GFP–X (X=indicated FIPs) and subsequently infected or mock-infected with PR8 at MOI 20. As a control, cells were co-transfected with mitoCherry and the GFP-tagged proteins (Fig. S1). At 14 h post infection, cells were fixed and processed for immunofluorescence staining of viral nucleoprotein (NP). Scale bars: 10 µm. (E,F) Colocalization between nucleoprotein and mitoRab11aCA (E) or nucleoprotein and mitoCherry (F), in the presence of GFP alone or GFP–FIPs or GFP–RBD, was plotted as described above. (G,H) Colocalization between GFP-tagged proteins and mitoRab11a (G) or mitoCherry (H) in mock-infected or infected cells, was plotted as above. Statistical analysis of data in B,C and E–H was performed using non-parametric Kruskal–Wallis test, followed by Dunn's multiple comparisons test (*P<0.05, **P<0.01, ***P<0.001). Experiments were performed twice and only a representative experiment is depicted. An average of 30 cells per experiment were analyzed. Horizontal red line represents the mean.

individual effectors and overcome redundancy between functional domains in FIPs. For this purpose, we fused Cherry–Rab11a (or Cherry as control) to the mitochondrial targeting sequence (MTS) of Tom20 (first 35 amino acids). These constructs are henceforward referred to as mitoRab11a and mitoCherry, respectively. We then validated the capacity of constitutively active (CA) and dominant-negative (DN) mitoRab11a to attract and bind to vRNPs. For this, we transfected HeLa cells with either of the mitoRab11a forms, or

Journal of Cell Science (2016) 129, 1697-1710 doi:10.1242/jcs.188409

mitoCherry, co-infected or mock co-infected cells with PR8 virus and quantified colocalization on confocal-acquired images. We observed that the MTS successfully targeted mitoRab11a CA, mitoRab11aDN or mitoCherry to the mitochondria because these colocalized with the mitochondrial protein Hsp60 (Fig. S1A and Fig. 3B, range of Pearson's correlations of 0.53±0.02 to 0.63±0.03, mean±s.e.m.). Furthermore, only mitoRab11aCA, and not mitoRab11aDN or the control, was able to recruit vRNPs at 14 h post infection (Fig. 3C, Pearson's correlation of 0.49±0.03 in comparison with negative correlations for mitoRab11aDN and controls). We have, thus, created an artificial system that involves targeting Rab11a to the mitochondria and is able to assess recruitment of vRNPs and Rab11a effectors.

To test whether FIPs and vRNPs competed for binding to Rab11a, we made use of this system. We co-transfected HeLa cells with GFP alone or GFP–FIPs, and mitoRab11a CA (or mitoCherry) and simultaneously infected or mock-infected these cells with PR8. We verified that mitoRab11a (Fig. 3D,G), but not mitoCherry (Fig. S1B, Fig. 3H), strongly colocalized with GFP–FIP1A, GFP–FIP1B, GFP–RCP (also called FIP1C), GFP–FIP2, GFP–FIP3, GFP–FIP5 and GFP–RBD (comprising the RBD of FIP5) (Fig. 3G), regardless of infection (Pearson's correlation lowest value of 0.55±0.05 for GFP–FIP5 mock), but not with GFP alone (Pearson's correlation of 0.30±0.05 for both mock and infected cells). For convenience, Fig. 3D and Fig. S1B show representative images of only two conditions – FIP2 and the RBD of FIP5. Moreover, mitoRab11a colocalized with viral nucleoprotein in the presence of GFP (Pearson's correlation of 0.48±0.03), but not in the presence of GFP–FIPs or GFP–RBD (Fig. 2E, highest Pearson's correlation of 0.07±0.02). As expected, no colocalization was detected between nucleoprotein and mitoCherry in the presence of GFP–FIPs or of the control GFP (Fig. 3F, highest Pearson's correlation among all conditions of 0.15±0.02). Taken together, these results indicate that full-length FIPs and not just the FIP RBDs compete for Rab11a binding to vRNPs.

vRNPs outcompete FIPs for binding to Rab11a during IAV infection

To substantiate the hypothesis that vRNPs outcompete FIPs for direct binding to Rab11a during infection, we measured the levels of FIP2 that co-purified with Rab11a, basing our choice on the availability of commercial antibodies. FIP2 was reported to bind exclusively to GTP-bound Rab11a, the same activated state that vRNPs attach to. We performed a pull-down assay over the course of infection using an antibody specific for Rab11a. We confirmed that total Rab11a levels did not vary during infection (Fig. 4A) (Amorim et al., 2011). The same trend was observed for input levels of FIP2 but not for nucleoprotein, PB2 and M1, which, as expected, gradually increased as infection progressed. In the samples that had been selectively precipitated with the Rab11a-specific antibody, PB2 (as proxy of vRNPs) was only detected in infected cells, and the levels increased during infection (Fig. 4A), corroborating findings that Rab11 is able to attach to vRNPs (Amorim et al., 2011, 2013; Eisfeld et al., 2011; Momose et al., 2011). Conversely, FIP2 was present in non-infected cells, and its intensity decreased as infection progressed. Interestingly, the reverse was observed in the unbound fraction (data not shown). As a control, the non-vRNP-associated viral protein M1 did not co-purify with Rab11a (Fig. 4A).

These results suggest that the interaction between active Rab11 and FIPs is inhibited by vRNPs in a mutually exclusive manner. We hypothesize that the lack of FIP binding to Rab11 vesicles during infection causes a decrease in sorting efficiency, by decreasing recruitment of molecular motors or proteins that promote membrane fusion. To prove that a causal relationship exists between the decrease in FIP binding and Rab11 redistribution, we designed a strategy to block the Rab11 domain that is responsible for binding to

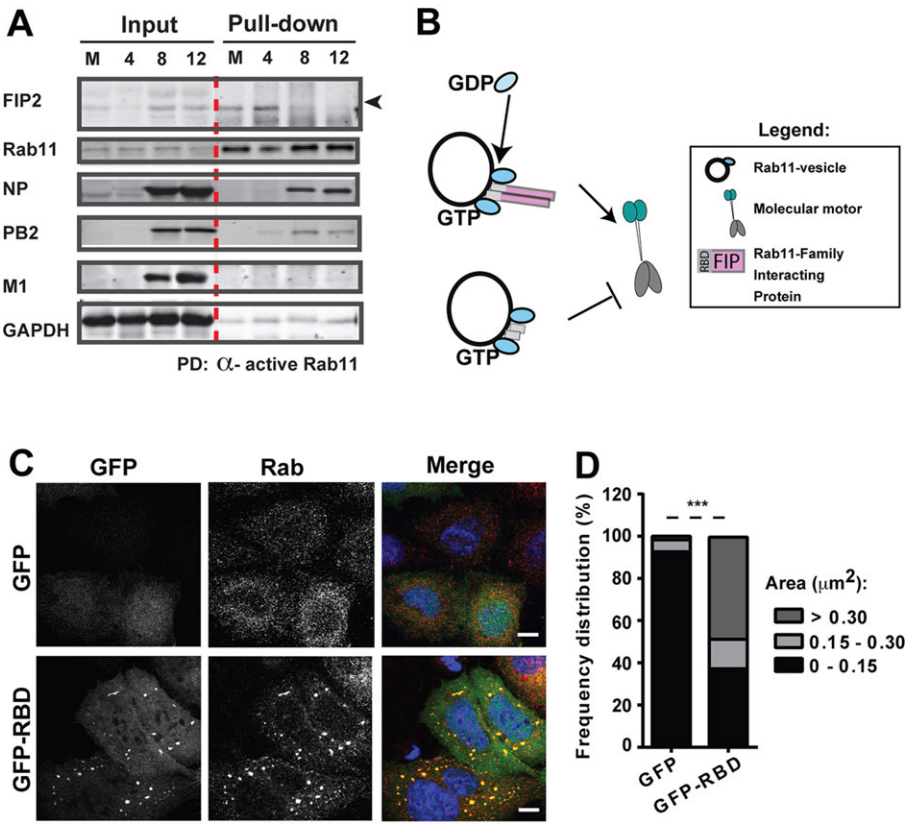

Fig. 4. FIP2 binding to Rab11 decreases during the course of IAV infection. (A) A549 cells were infected or mock-infected with PR8 at MOI 3. At the indicated time points, cells were lysed (10% input) and GTP-bound Rab11 was pulled-down from the cell lysates. Bound proteins (pull down) and total proteins (input) were detected by western blotting. M, mock. (B) Experimental strategy for testing for a causal relationship between impeding Rab11 vesicular sorting and Rab11 redistribution. Activated Rab11, upon GDP-GTP exchange, recruits molecular motors for efficient sorting. When the RBD of FIP5 is supplied exogenously, it blocks access of Rab11a to molecular motors. (C) HeLa cells were transfected with GFP alone or GFP–RBD for 14 h. Cells were then fixed and processed for immunofluorescence staining of Rab11a (Rab). Scale bars: 10 µm. (D) The frequency distributions (%) of small, medium and large Rab11-vesicle areas (µm^2) were plotted over the course of infection. Statistical analysis of data was performed using two-way ANOVA followed by a Bonferroni's multiple comparisons test (***P<0.01). The graph shows a pool of data from two independent experiments. An average of 20 cells per experiment were analyzed.

Journal of Cell Science (2016) 129, 1697-1710 doi:10.1242/jcs.188409

FIPs. We used uninfected cells to overexpress a truncated FIP bearing solely the RBD, which is able to bind to Rab11 but not to molecular motors (Fig. 4B), thus mimicking our predictions about the recycling endosome upon infection. We found that overexpression of GFP–RBD, but not of GFP (used as control), caused a redistribution of Rab11 vesicles that, with confocal microscopy analysis, resulted in enlarged puncta (Fig. 4C). The size of Rab11 vesicles was quantified as above, and an increase of 48.5% in large vesicles was observed at 24 h post transfection, mimicking Rab11 alterations during infection (compare Fig. 4D with Fig. 1C). In summary, our results point to a model where vRNPs outcompete FIPs for Rab11a binding, leading to Rab11 redistribution.

Membrane remodeling during IAV infection can be analyzed by performing correlative light and electron microscopy using cells that stably overexpress Rab11a

We then sought to observe at an ultrastructural level how Rab11 membranes organize during infection. Several mechanisms could explain an increase in Rab11 puncta. One process is vesicular clustering, suggested by Eisfeld et al. (2015), mediated by stalling vesicular sorting at any step during trafficking. Similarly, alterations in fusion and fission events on colliding vesicles could promote the increase in vesicle size. These hypotheses, distinguishable by ultrastructural studies, are important to discriminate between because they correspond to different biological processes. The characterization of alterations in Rab11 vesicles could be accomplished by performing transmission electron microscopy that preserves delicate ultrastructure. However, vRNPs and Rab11 lack electron density for detection by this method. Because vRNPs in the cytoplasm are found attached to Rab11 vesicles (Amorim et al., 2011) and the recycling endosome only suffers alterations if bound to vRNPs (Fig. 1A), we could in theory differentiate between infected and uninfected cells using stable cell lines expressing GFP–Rab11a, and apply correlative light and electron microscopy (CLEM). This technique combines methods to mark viral and host proteins by fluorescence with the powerful resolution of electron microscopy to visualize cellular architecture, including budding virions. The strategy of using CLEM on Rab11-expressing stable cell lines is not devoid of problems that need to be tightly controlled. First, it has been reported that exogenous expression of Rab11 leads to increased recycling endosomes that could mask the effects of IAV infection (Rink et al., 2005; Stenmark et al., 1994). To assess whether GFP–Rab11-expressing A549 cell lines produced comparable Rab11a alterations, we quantified vesicle size upon infecting both systems (Fig. S2). In mock-treated cells, the frequency distribution of large vesicles was 5.6±3.4 and 11.5±2.2 (mean±s.e.m.) for A549 cells and A549 cells expressing GFP-tagged wild-type Rab11 (GFP–Rab11aWT), respectively (Fig. S2D). These values indicate an increase in larger vesicles upon transduction of Rab11. However, infected cells showed more vesicles in the larger size category (24.9±4.8% and 46.6±12.1%, for A549 cells and GFP–Rab11WT-expressing A549 cells at 8 h, respectively; Fig. S2D), indicating that indeed Rab11 provides the differentiating signature to identify infected cells. Additionally, the frequency distribution of large Rab11a vesicles increased as infection progressed in GFP–Rab11aWT-expressing and A549 cells, becoming statistically significant for both cell lines at 8 h post infection (Fig. S2D). We also compared the progression of infection in the cell lines by using plaque assays. We observed that viral production was identical between both cell lines and increased from 6 h to 14 h post infection (Fig. S2B), without affecting nucleoprotein expression (Fig. S2C). Overall, we conclude that cells that stably overexpress the Rab11aWT protein behave in a manner similar to that of A549 cells, with regards to Rab11a redistribution upon infection and viral production. Hence, these cells are suitable for further characterizing infection-induced alterations to Rab11a-positive structures. We also conclude that CLEM is technically complex. It is widely recognized that the replacement of water with resin, during sample processing for electron microscopy, induces cell deformations. Therefore, a perfect superimposition of confocal and electron microscopy images is simply not attainable (Loussert Fonta and Humbel, 2015). Furthermore, because our protocol required epon resin, inclusion of fiduciary landmarks to help alignment was not feasible. To superimpose confocal and electron microscopy images, we used *z*-stacks of the same cell grown in gridded coverslips (Fig. S3). Using the *z*-information from the optical sectioning of the confocal data and from the physical sectioning of the electron microscopy data, we obtained a rough alignment of these two stacks (Fig. S3). Features like cell-to-cell contact (see arrows in Fig. S4A); contours of the cell membrane; size, shape and orientation of the nucleus; as well as small structural details like holes in cell edges, were used to do a more refined alignment between the confocal and electron microscopy data (Fig. S4A,B). Features like the microtubule organizing center (MTOC), easily detected in both systems, was used to validate this alignment. For this, we examined Rab11a accumulation at the perinuclear region with confocal analysis (Amorim et al., 2011) to successfully predict the location of the centrioles in electron microscopy images (see asterisks in Fig. S4A and C).

To demonstrate the accuracy of the CLEM alignments, we thought of using a strategy that altered the distribution of Rab11 vesicles, far more than normal infection, therefore artificially creating dramatic 3D forms that span the entire volume of the cell (Amorim et al., 2013). If the forms captured by confocal microscopy matched in shape and volume the ultrastructural features found in electron micrographs, our system would be validated. 3D forms of Rab11 vesicles can be induced by a drug called nucleozin (Kao et al., 2010). We have previously shown that when added late in infection, nucleozin blocks otherwise transitory Rab11 vesicular interactions, on account of its binding affinity for several domains on nucleoprotein, a protein that coats vRNPs. By this method, individual vRNPs are ‘stuck’ by nucleozin, causing their aggregation in the cytoplasm (Fig. 5C, and for detailed description on nucleozin readers are referred to Amorim et al., 2013). Furthermore, because nucleozin has affinity for nucleoprotein and not Rab11, its action is specific to infected cells. Interestingly, the 3D forms created included Rab11 and vRNPs but excluded markers from several organelles, including GM130 (Golgi) and calnexin (endoplasmic reticulum) (Amorim et al., 2013). By performing confocal inspection, infected cells exhibited 3D forms of Rab11–vRNP vesicles (Amorim et al., 2013) upon nucleozin incubation (Fig. 5A,B). Infection was confirmed, by performing electron microscopy, by the presence of budding virions (Fig. 5A, inset 3). Inspection of sequential electron microscopy sections showed (1) shapes that resembled those acquired for GFP–Rab11aWT by confocal analyses (see dashed lines in Fig. 5) and (2) shapes that comprised dramatic agglomerates of vesicles of variable sizes (compare A and B in Fig. 5). An advantage of using this method is the extensive volume that nucleozin-induced 3D forms occupy in the cell that can be observed through many consecutive slices in the *z*-stacks in both confocal and electron microscopy images, which displayed only minor changes (Fig. 5). Our data strongly indicate an accurate alignment in the images obtained by using both methods, where ultrastructural signatures of infection can be detected with electron microscopy, matching those observed with confocal microscopy.

Journal of Cell Science (2016) 129, 1697-1710 doi:10.1242/jcs.188409

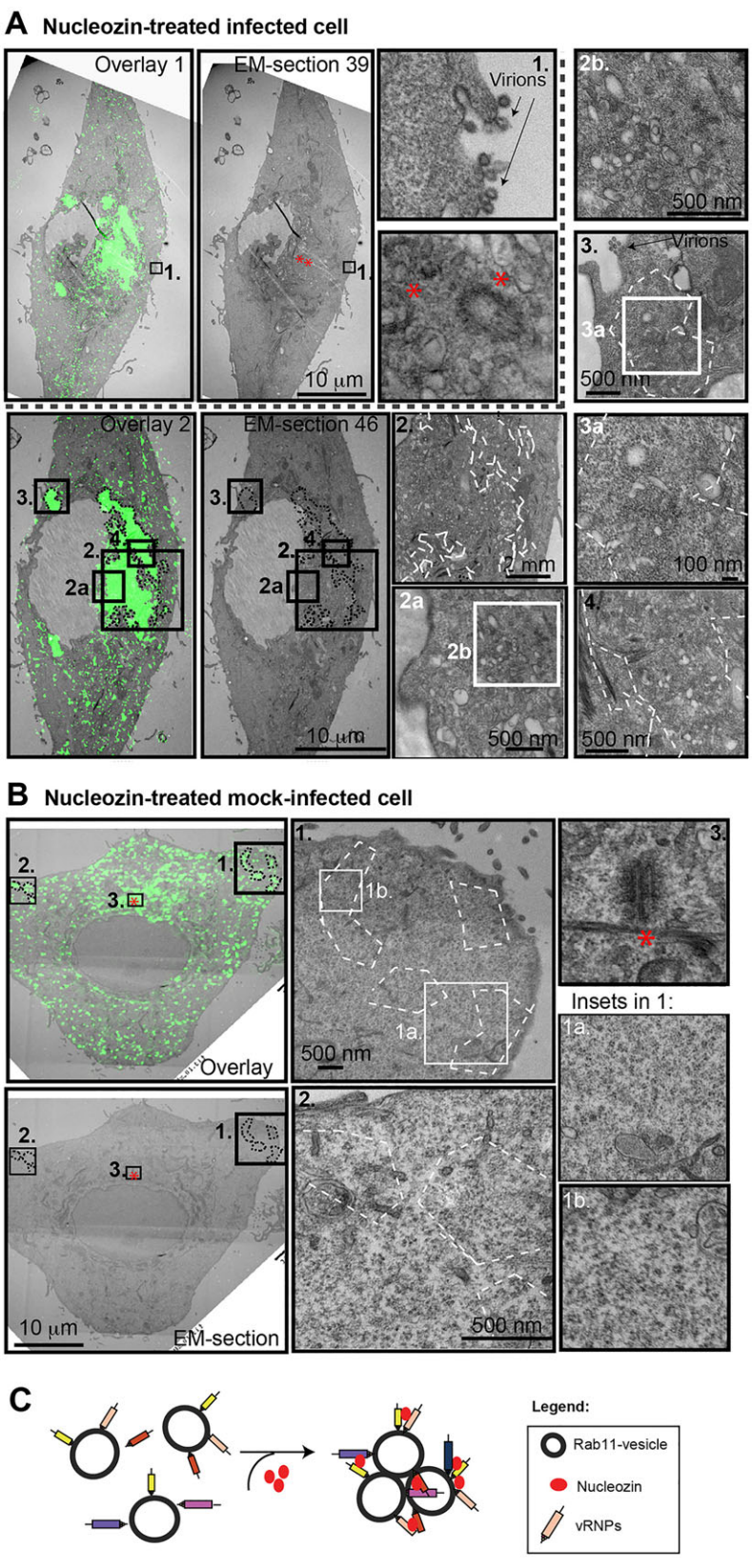

Fig. 5. IAV infection, in the presence of nucleozin, causes aggregation of Rab11–vRNP-carrying vesicles, which can be observed in electron microscopy images. GFP–Rab11aWT cells were infected (A) or mock-infected (B) with PR8 at MOI 3. Cells were treated with 2 μM nucleozin at 6 h post infection, fixed at 8 h post infection and processed for CLEM analysis. Overlay refers to a montage of two sections from the same cell imaged by using confocal and electron microscopy [shown adjacent, electron micrograph (EM) sections 39 and 46]. In A, image 1 shows regions of interest selected from the overlay 1 and areas 2–4 in overlay 2. GFP–Rab11a areas are highlighted with dashed lines. Centrioles to mark the MTOC were found, overlay 1 (asterisks). Insets in images 2 and 3 detail regions of interest of overlay 2 (2a and 3a). An additional magnified region of image 2a is shown (2b). Budding virions were highlighted to show that the cells were infected. In B, images 1 and 2 show areas of interest of the overlay. Zoomed areas of image 1 are also shown (inset 1a and 1b). Image 3 shows centrioles that mark the MTOC (asterisk). Note that this region corresponds in the overlay image to a perinuclear region where Rab11 accumulates, which has been previously shown to surround γ-tubulin, which is the MTOC marker (Amorim et al., 2011). The experiment was performed three times. (C) Scheme of the mode of action of nucleozin (red dot). Nucleozin binds to three domains in nucleoprotein, even when nucleoprotein is bound to RNA in vRNPs. Hence, when vesicles transporting vRNPs collide, nucleozin induces a stable interaction between them, forcing the formation of prominent aggregates.

Ultrastructural inspection reveals that IAV infection leads to clustering of heterogeneous Rab11a- and vRNP-positive vesicles of single and double membranes

Our goal was to detect alterations in recycling endosome membranes during infection. Therefore, we infected and mock infected cells for 8 h, before confocal acquisition of *z*-stacks and processing for electron microscopy analysis. Cells of interest were successfully infected, as determined by the observation of enlarged Rab11a green puncta in confocal images (Fig. 6A, overlay) and budding virions in electron micrographs (Fig. 6A, inset 3). Ultrastructural inspection of the refined alignment between electron micrographs and confocal *z*-stacks revealed that, at 8 h

Journal of Cell Science

Journal of Cell Science (2016) 129, 1697-1710 doi:10.1242/jcs.188409

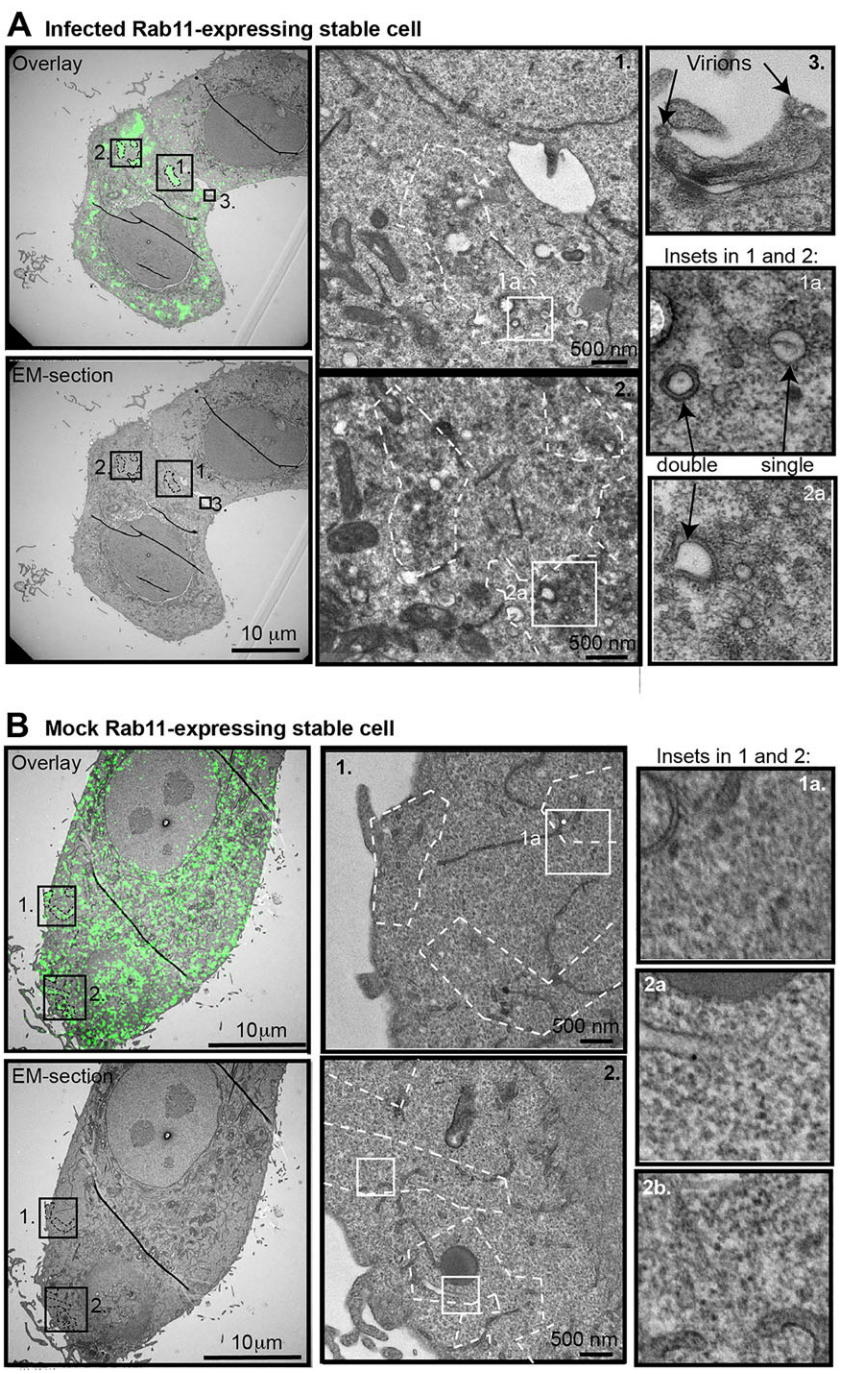

Fig. 6. IAV infection induces membrane rearrangements resulting from the formation of clustered vesicles of single and double membranes positive for Rab11a. Cells stably overexpressing GFP–Rab11a were infected (A) or mock-infected (B) with PR8 at MOI 3. At 8 h post infection, cells were fixed and processed for CLEM analysis. Overlay refers to a montage of sections from the same cell imaged by confocal and electron microscopy (shown below, EM-section). Images 1 and 2 detail regions of interest selected from the overlay where GFP–Rab11a areas are marked with a dashed line. In A, insets 1a and 2a refer to images 1 and 2, where vesicles formed by single and double membranes are marked. In image 3, budding virions are highlighted, confirming that the cell was infected. In B, insets 1a, 1b and 2a correspond to areas positive for GFP–Rab11a in images 1 and 2. Note that vesicular clustering was not detected. Experiments were performed at least three times.

post infection, the areas positive for GFP in confocal microscopy images matched to sets of clustered vesicles (Fig. 6A, insets 1,2). Interestingly, these membrane rearrangements contained clustered vesicles of single and double membranes that were of variable sizes (Fig. 6A, insets 1a,2a), which were absent in mock-infected cells (Fig. 6, compare A with B). The membranous clusters detected were scattered in the cytoplasm in areas close to the surface (Fig. S4). This observation is in agreement with a putative staging area containing Rab11a and vRNPs found beneath the plasma membrane (Amorim et al., 2011; Eisfeld et al., 2011) that has been postulated to be formed by agglomerates of multiple transport intermediates (Eisfeld et al., 2011). We have confirmed this hypothesis but found that the nature of membranes varied from single and double and were heterogeneous, suggesting additional biological processes altering their morphology.

To further corroborate our results, we performed the same CLEM alignment on cells where the viral genome (using GFP–nucleoprotein as proxy), instead of Rab11a, was marked. HeLa cells were concurrently transfected with GFP–nucleoprotein and infected with PR8. This method has been established and characterized previously (Amorim et al., 2013), but for clarity will be briefly explained here. In uninfected cells, GFP–nucleoprotein, which contains several nuclear localization signals, is found exclusively in the nucleus. At later stages of infection, GFP–nucleoprotein migrates partly to the cytoplasm in puncta that are positive for vRNAs and all the viral polymerase subunits (Amorim et al., 2013). It was concluded that this system could be used to track vRNPs, as nucleoprotein could only be found in the cytoplasm of infected cells (Amorim et al., 2013). Using this method and CLEM, we could detect infected cells, as confirmed by

Journal of Cell Science (2016) 129, 1697-1710 doi:10.1242/jcs.188409

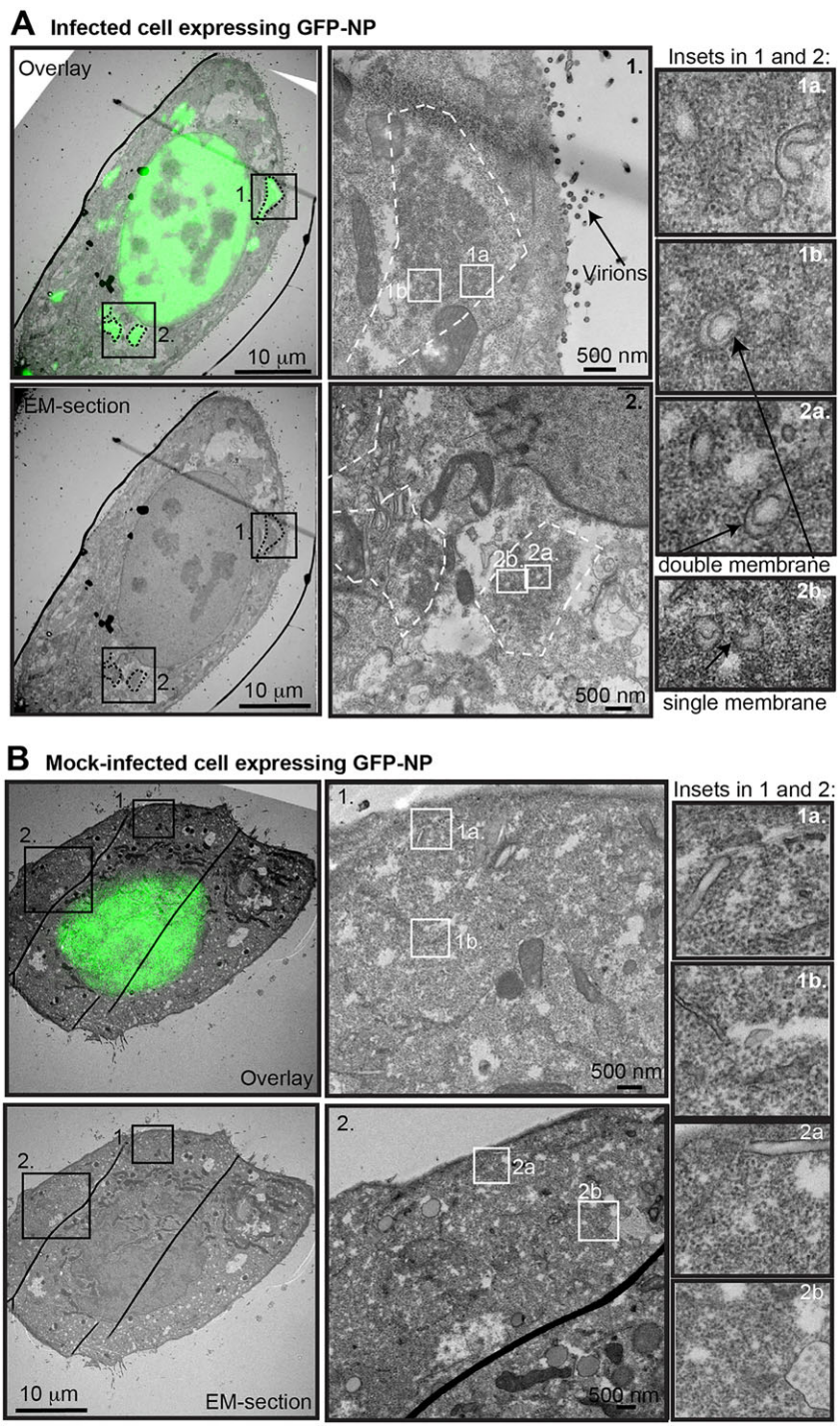

Fig. 7. IAV infection induces membrane rearrangements resulting from the formation of clustered vesicles with single and double membranes positive for vRNPs. HeLa cells were transfected with GFP–nucleoprotein (GFP–NP) and infected (A) or mock-infected (B) with PR8 at MOI 5. After 14 h, cells were fixed and the cell of interest was imaged by performing confocal and electron microscopy to produce the image shown as the overlay. In A, images 1 and 2 detail regions of interest selected from the overlay where GFP–nucleoprotein areas are marked with a dashed line. Budding virions are highlighted in image 1, confirming that the cell was infected. In A, insets 1a, 1b, 2a and 2b correspond to magnified regions in images 1 and 2, where vesicles formed by single and double membranes are marked. In B, images 1 and 2 detail regions in the corresponding overlay that were not positive for GFP–nucleoprotein because, in uninfected cells, this protein was not found outside of the nucleus. These regions show no specific vesicular clustering and serve as control. Experiments were performed at least twice.

nucleoprotein staining in the cytoplasm with confocal microscopy and budding virions in electron micrographs (Fig. 7A, overlay and inset 1). By using electron microscopy, similar features of cytoplasmic nucleoprotein staining could be detected that were similar to those observed in the CLEM analysis for GFP–Rab11a in Fig. 6. Areas positive for GFP–nucleoprotein corresponded to clusters of vesicles of diverse sizes (Fig. 7A, insets 1,2). Furthermore, and as above, closer inspection of these clusters revealed that these were formed by a mixture of single and double membranes. We also found several U-shaped single-membraned vesicles (see Fig. 7A, inset 1a) and open double-membraned vesicles. Mock-infected cells did not exhibit areas of nucleoprotein in the cytoplasm when observed by using confocal microscopy and, upon inspection of cytoplasm with electron microscopy, the cells showed no visible clusters of vesicles of any sort (Fig. 7B).

DISCUSSION

The genome of IAV is divided into eight segments. Segmentation imposes a problem on viral assembly, because eight-segment vRNPs need to meet in order to form an infectious virion. Although supramolecular assembly of vRNP complexes could take place at the surface, several reports suggest that it occurs en route to the plasma membrane (Chou et al., 2013; Eisfeld et al., 2011; Lakdawala et al., 2014; Momose et al., 2011). In this paper, we

Journal of Cell Science (2016) 129, 1697-1710 doi:10.1242/jcs.188409

provide the molecular basis underlying a viral-induced mechanism to alter host recycling efficiency that promotes vesicular clustering and originates from the Rab11-dependent vRNP hotspots previously described (Chou et al., 2013; Lakdawala et al., 2014). We show that vRNP binding to Rab11, and no other viral component, induced alterations in Rab11 distribution (Figs 1A–C and 2), and that infection decreased recycling of transferrin (Fig. 1D). Biochemical analyses, using an artificial targeting system and pull-down assays, further indicated that vRNPs and FIPs competed for Rab11a binding (Figs 3, 4; Fig. S1). Subsequently, we showed that, in uninfected cells, alterations in Rab11a distribution could be provoked by impeding Rab11 access to molecular motors (and consequently downstream steps in trafficking), which indicates that there is a causal relationship between all these variables (Fig. 4C,D). At this point, we can only speculate that this impairment could expand to other GTP-Rab11 effectors, and additional experiments are required for clarification.

We propose the model in Fig. 8 to explain the delivery of vRNPs to the plasma membrane during infection with IAV. When vRNPs start being exported from the nucleus, reaching the cytosol in low concentrations, there is sufficient free Rab11a to recruit FIPs and/or other effectors to promote efficient vesicular sorting using the microtubule network, as shown by others previously (Amorim et al., 2011; Momose et al., 2007). Conversely, at later stages, higher levels of vRNPs reach the cytosol, free Rab11 levels decrease and FIP recruitment is reduced. This reduction leads to an alteration in Rab11 vesicular sorting that can operate at the level of movement and/or any downstream event in trafficking, such as fusion with the cell surface. The identification of the blocked step requires studying other Rab11 effectors. The reduction in FIP recruitment, nevertheless, results in vesicular clustering. Consistently, we report, for the first time, ultrastructural features of Rab11a vesicles over the course of infection. Using CLEM, we showed that infection induced the appearance of clustered heterogeneous vesicles scattered in discrete locations in the cytoplasm, comprising single and double membranes that were positive for Rab11a and vRNPs (Figs 5–7; Figs S3 and S4). These vesicles harbored coiled-coil string-like structures protruding towards the cytoplasm that could correspond to vRNPs (Noda et al., 2006; Sugita et al., 2013; Fournier et al., 2012). Although vesicular clustering might, at some level, be in agreement with the reduction of recycling endosome efficiency that we report here, the existence of vesicles with double membranes suggests a distinct mechanism to rearrange membranes that we have not addressed and might be related to lipid metabolism. Interestingly, very recently, cholesterol has been shown to be enriched in recycling endosome vesicles (Kawaguchi et al., 2015). The formation of double-membraned vesicles is unclear; however, we found several U-shaped single-membraned vesicles (see Fig. 7A, inset 1a) and open double-membraned vesicles (Fig. 7, inset 1b). Vesicles shaped in this way have been described as appearing in chronological order in rosette-like structures observed during poliovirus infection (Belov et al., 2012). It is also unknown whether the proportion of double-membraned vesicles increases with infection and the role, if any, that they play.

Creation of Rab11-dependent vRNP hotspots through the mechanism that we propose could in principle facilitate assembly of the genomic core (Chou et al., 2013). Induction of vesicular clustering and concentration of viral material for facilitated viral production is a well-known mechanism that operates in many positive-sense RNA viruses and poxviruses (Limpens et al., 2011; Monaghan et al., 2004; Welsch et al., 2009; Laliberte and Moss, 2010). Nevertheless, this hypothesis, as appealing as it might be, awaits compelling experimental support because, at the moment, the relevance of the clustered Rab11 vesicles is still uncertain. Very recently, however, it has been shown that SeV, a non-segmented RNA virus, alters the distribution of Rab11 during the course of infection. This observation supports a functional role for the clusters, instead of them being a byproduct of infection, given that the assembly of the SeV genome deviates from that of a segmented genome, but the SeV altered distribution of Rab11 might reflect the need to concentrate other virion components (Stone et al., 2015). Other roles found for vesicular clustering originating during infection with different types of virus include the formation of structures for escaping host anti-viral responses or for recruiting membrane, which is a pre-requisite for the budding of enveloped virions (Harak and Lohmann, 2015; Laliberte and Moss, 2010;

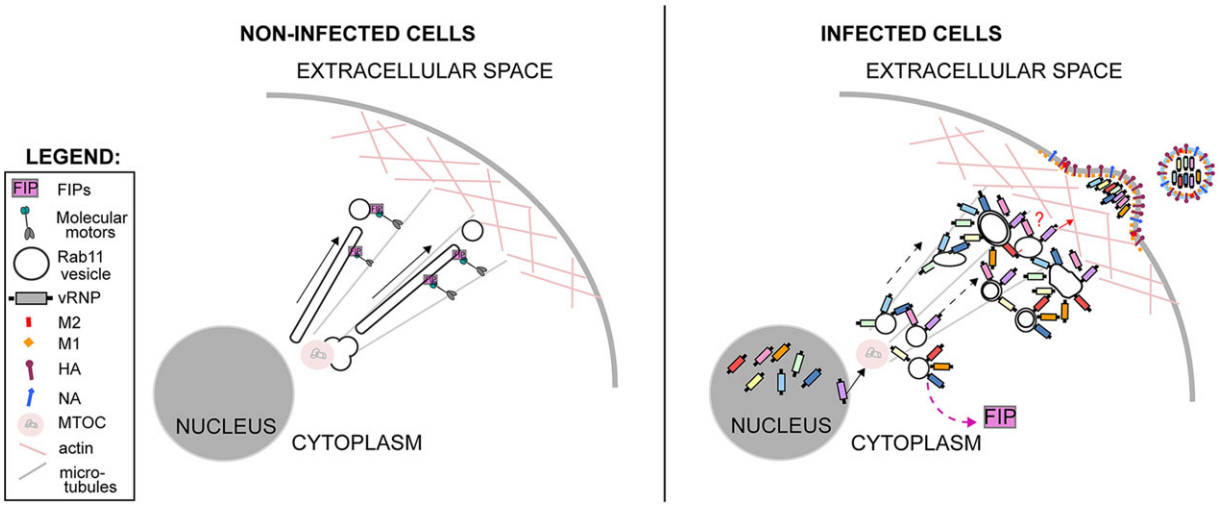

Fig. 8. Proposed model of IAV-induced Rab11a vesicle aggregation. In uninfected cells, activated Rab11a is able to attract different FIPs that facilitate the binding of a set of molecular motors and transport vesicles, along the microtubule and actin cytoskeleton, to the surface where they fuse. During infection with IAV, vRNP binding to Rab11a vesicles competes with Rab11a effectors, including FIPs. Such competition leads to a reduction in the levels of Rab11 effectors that are deposited in these membranes, stalling the recycling process (in an unknown step). The slow down in vesicular sorting results in the clustering of vesicles with single and double membranes, creating hotspots of vRNPs. Complete or incomplete supramolecular complexes reach the plasma membrane by a yet unclear process involving direct or indirect transfer of vRNPs from Rab11a vesicles.

Journal of Cell Science

Journal of Cell Science (2016) 129, 1697-1710 doi:10.1242/jcs.188409

Lindenbach and Rice, 2013). Whether any of these functions apply for IAV infection is currently under investigation.

The subsequent step in viral assembly is the delivery of vRNPs to the inner side of the apical plasma membrane from where virions bud. At least two models could explain this step: (1) direct fusion of vRNP-carrying vesicles with the plasma membrane or (2) the transfer of vRNPs from Rab11a vesicles to an acceptor molecule. Direct fusion of Rab11 vesicles with the cell surface, without prior formation of intersegment interactions, does not seem to mediate this process, for several reasons: (1) the low abundance of Rab11a inside virions (Hutchinson et al., 2014; Shaw et al., 2008), (2) the lack of Rab11a colocalization with nucleoprotein at the plasma membrane (Eisfeld et al., 2011) and (3) recent findings demonstrating that not all vRNPs are accommodated in virions in a head-to-tail orientation (Sugita et al., 2013). Conversely, the recycling endosome has been proposed to work as a transient station (Eisfeld et al., 2015). Transfer of vRNPs requires switching off Rab11a. So far, no host factor has been unequivocally shown to facilitate vRNP unbinding from Rab11a vesicles. However, many have been identified as bona fide facilitators of viral assembly and budding: CD81 (He et al., 2013), F1F0-ATPase (Hui and Nayak, 2001; Gorai et al., 2012), RACK1 (Demirov et al., 2012) and G-protein kinase(s) (Hui and Nayak, 2002). Viral proteins could also be involved in the process. The interaction of vRNPs with M1 (Elster et al., 1997; Noton et al., 2007; Ye et al., 1999; Avalos et al., 1997), and oligomerization of M1 (Harris et al., 2001; Zhang et al., 2015; Zhao et al., 1998) with the transmembrane proteins M2 (Chen et al., 2008; McCown and Pekosz, 2006), HA and neuraminidase (Barman et al., 2001; Enami and Enami, 1996) could, in principle, promote vRNP progression from the recycling endosome. These hypotheses need further investigation in order to further understanding of viral assembly and also the emergence of reassortant viruses.

MATERIALS AND METHODS

Human epithelial cells [embryonic kidney 293T or 293ET (gift from Dr Colin Adrain, Instituto Gulbenkian de Ciência, Portugal)], cervical HeLa, alveolar basal cells (A549) and Madin-Darby canine kidney cells (MDCKs) were cultured as described previously (Amorim et al., 2011). All cells, except the 293ET lines, were a kind gift from Professor Paul Digard, Roslin Institute, UK. All cells were regularly tested for mycoplasma contamination. Reverse-genetics derived A/Puerto Rico/8/34 (PR8; H1N1) was used as a model virus (de Wit et al., 2004) and titrated as described previously (Matrosovich et al., 2006). Virus infections were performed at a multiplicity of infection (MOI) of 3 to 20, as described previously (Amorim et al., 2011). After 30 min, cells were overlaid with Dulbecco's modified Eagle's medium (DMEM) containing 0.14% bovine serum albumin. The drug nucleozin (Kao et al., 2010) (Professor Richard Kao, University of Hong Kong, China), dissolved in DMSO, was used at a final concentration of 2 µM, and LMB, dissolved in ethanol, was used at 10 nM (Elton et al., 2001; Ma et al., 2001). Reverse genetic plasmids were contributed by Dr Ron Fouchier, Erasmus Medical Center, The Netherlands.

Stable cell line production

Plasmid encoding GFP-tagged Rab11aWT was used to produce a lentiviral plasmid version by PCR amplifying and cloning the GFP–Rab11aWT insert into BamHI–NotI restriction sites in the multi-cloning site of pLEX.MCS vector (Thermo Scientific). Primers 5′-TCAGGGATCCACCATGGTGA-GCAAGGGCGAG-3′ (GFP forward) and 5′-TCAGGCGGCCGCTTAG-ATGTTCTGACAGCACTGC-3′ (Rab11a reverse) were used for insert amplification by PCR. 293ET cells were transfected with VSV.G, psPAX2 and pLEX.GFP-Rab11aWT using Lipofectamine 2000 (Life Technologies) and OptiMEM (Life Technologies), according to manufacturer's instructions. Lentiviral particles were collected after 4 days and stored at −80°C. These were used to transduce A549 cells for 24 h; cells were then positively selected for 48 h with 2.5 µg/ml puromycin (Calbiochem, Merck Millipore, 540411). The GFP–Rab11aWT cell lines were passaged six times before use and kept in culture medium that had been supplemented with 1.25 µg/ml puromycin.

Plasmids produced during this study

GFP–FIPs

Plasmids encoding GFP-tagged FIPs were produced by PCR-amplification of cDNA from HeLa cells and cloning FIP1A, FIP1B and FIP1C (RCP) into XhoI–BamHI restriction sites, FIP2 into EcoRI–BamHI, FIP4 into KpnI–EcoRI or FIP5-RBD into EcoRI–KpnI in pEGFP-C2 (Clontech). GFP–FIP3 and FIP5 were a gift from Dr Duarte Barral, Centro de Estudos de Doenças Crónicas, Portugal. The following primers were used: FIP1A forward: 5′-TCGACTCGAGCATGGGCAGGACCCGTG-3′; FIP1B/RCP forward: 5′-TCGACTCGAGCATGTCCCTAATGGTCTCGGC-3′; FIP1A and FIP1B/RCP reverse: 5′-TCGAGGATCCGTTACATCTTTCCTGCT-TTTTTGC-3′; FIP2 forward: 5′-TCGAGAATTCATGATGCTGTCCGA-GCAAGC-3′; FIP2 reverse: 5′-TCGAGGATCCGTTAACTGTTAGAGA-ATTTGCCAGCTT-3′; FIP4 forward: 5′-TCGAGAATTCATGGCGGGC-GGCGCGGGCTGG-3′; FIP4 reverse: 5′-TCGAGGTACCCTTAGTGTT-TGATCTCGAGGATGG-3′; FIP5 RBD forward: 5′-TCGAGAATTCGG-CCCCCCAGGCTGGCCAGAT-3′; FIP5 RBD reverse: 5′-TCGAGGTA-CCCCTATTTGGGGGGGCCCGGGGGGATCT-3′.

MitoCherry-Rab11a constitutively active and dominant-negative plasmids encoding Cherry–Rab11aCA or Cherry–Rab11aDN were produced by cloning Rab11aCA or DN inserts into pCherry-C2 vector using EcoRI–BamHI restriction sites. Primers used were: Rab11aCA forward: 5′-ATGCGAATTCATGGGGACCCGGGAC-3′; Rab11aCA reverse: 5′-ATGCGGATCCTCACAGGTTCTGGCAGCA-3′; Rab11aDN forward: 5′-GAGATTCTGGTGTTGGAAAGAATAATCTCCTGTCTC-GATTTAC-3′; Rab11aDN reverse: 5′-GTAAATCGAGACAGGAGATT-ATTCTTTCCAACACCAGAATCTC-3′.

The first 105 base pairs of the Tom20 MTS were amplified and cloned upstream of Cherry–Rab11aCA using NheI–AgeI sites. The following primers were used: Tom20 tag forward: 5′-ATGCGCTAGCATGGTGG-GTCGGAACAGC-3′ and Tom20 tag reverse: 5′-ATGCACCGGTTTGA-AGTTGGGGTCACTTCG-3′.

For the mitoCherry Rab11aDN plasmid, the Cherry sequence from Cherry–Rab11aDN was replaced by the Tom20-Cherry tag from mitoCherry–Rab11aCA. The Tom20–Cherry tag was cloned upstream of Rab11aDN using NheI–XhoI sites.

Microscopy

Confocal

Immunofluorescence assays were performed as described previously (Simpson-Holley et al., 2002). Antibodies used were: rabbit polyclonal against Rab11a (1:100; Life Technologies, 715300) and Hsp60 (1:200; Abcam, ab31115); mouse monoclonal against nucleoprotein (1:1000; Abcam, 20343). Secondary antibodies were all from the Alexa-Fluor range (1:1000; Life Technologies). Single optical sections were imaged with a Leica SP5 live or inverted confocal microscope and post-processed using ImageJ (National Institutes of Health; NIH) software to quantify vesicle area and calculate Pearson's correlation coefficients. For vesicle-size analysis (area in μm^2), images were converted to 8-bit color and a 'background subtraction' of 20 pixels applied. Subsequently, 'threshold' was adjusted to 14 (lower level) – 255 (upper level), followed by using the 'analyze particle' function to quantify each vesicle inside selected cells. Frequency distributions were calculated and plotted with GraphPad Prism using intervals of 0–0.15, 0.15–0.30 and above 0.30 μm^2. To calculate Pearson's correlation coefficient, the 'Coloc 2' function of ImageJ was used, and values were plotted using GraphPad Prism.

Correlative light and electron microscopy

Fluorescently labeled cells seeded onto gridded dishes (MatTek Corporation, P35G-2-14-C-GRID) were infected and treated with nucleozin when appropriate. At indicated times, cells were fixed with 2% paraformaldehyde, 1% glutaraldehyde, 0.1% malachite green dye in 0.2 M

PHEM buffer (5 mM HEPES, 60 mM PIPES, 10 mM EGTA, 2 mM $MgCl_2$; pH 7.4) for 10 min at 37°C. An incubation in 4% paraformaldehyde, 0.5% glutaraldehyde, 0.05% malachite green dye in 0.1 M PHEM (pH 7.4) was then performed for 35 min at room temperature. Samples were washed twice with 150 mM glycine for 10 min at room temperature and kept in 0.1 M PHEM buffer (pH 7.4) until confocal imaging. Upon confocal imaging, samples were fixed with 2.5% glutaraldehyde, 0.05% malachite green dye in 0.1 M PHEM (pH 7.4) for 20 min at room temperature. Samples were then extensively washed in PHEM buffer and post-fixed with 0.8% potassium ferricyanide and 1% osmium for 30 min, on ice, in the dark. Further staining with 1% tannic acid for 20 min on ice preceded an incubation in 0.5% uranyl acetate for 1 h at room temperature, with extensive washes in water in between steps. After dehydration with increasing percentages of ethanol, samples were embedded in epon resin. Images of the regions of interest were acquired with a Hitachi H-7650 transmission electron microscope.

Transferrin uptake and recycling assay

Infected or mock-infected cells were serum-starved in serum-free DMEM. Cells were incubated with transferrin-conjugated to Alexa-Fluor-647 (1:50; Life Technologies, T-23366) for 10 min at 37°C, 5% CO_2. After this period, cells were quickly washed with PBS and either fixed with 4% paraformaldehyde (to quantify uptake) or kept for another 10 min in complete DMEM before fixation (to quantify recycling). Cells were imaged with confocal microscopy, and the efficiency of recycling was determined by subtracting the signal intensity detected at the uptake and recycling steps. Signal intensity (mean gray value) was quantified by using the 'Analyze Particle' function of ImageJ (NIH) software.

Pull-down and western blotting

Pull down of GTP-bound Rab11a was performed using the Rab11 activation assay kit (Abcam, 173255). A549 cells, confluent in 10-cm dishes, were infected or mock infected. At indicated times, cells were lysed in 1 ml of the provided lysis buffer containing 1 mM phenylmethylsulfonyl fluoride and protease inhibitor cocktail (Roche) on ice for 30 min. Clarified samples were incubated overnight at 4°C with 1 µl of anti-active-Rab11 monoclonal antibody (Abcam, 173255) plus 20 µl of A/G agarose beads. Pelleted beads were washed extensively with lysis buffer and bound proteins were eluted by boiling in SDS-PAGE buffer containing 2.5% β-mercaptoethanol.

Western blotting was performed according to standard procedures and imaged using a LI-COR Biosciences Odyssey near-infrared platform, as described previously (Bruce et al., 2009). Antibodies used included rabbit polyclonals against FIP2 (1:250; Abcam, 76892), Rab11 (1:500; Abcam, 78337), PB2 (1:1000; gift from Professor Paul Digard; validated in Amorim et al., 2013); mouse monoclonals against virus nucleoprotein (1:1000; Abcam, 20343); goat polyclonals against GFP (1:2000; Sicgen, AB0020), GAPDH (1:2000; Sicgen, AB0049) and M1 (1:500; ab20910). The secondary antibodies used were from IRDye range (1:10,000; LI-COR Biosciences).

Acknowledgements

The authors acknowledge Professor Paul Digard (Roslin Institute, UK) for providing reagents (antibodies, cell lines, viral strains and plasmids), and Dr Ron Fouchier (Erasmus, The Netherlands) for the reverse-genetics plasmids. The authors thank Professor Stephen Cusack (European Molecular Biology Laboratory, France) for helpful discussions.

Competing interests

The authors declare no competing or financial interests.

Author contributions

S.V.-C. planned and performed experiments, analyzed data and wrote the manuscript; M.A. and B.K. performed experiments; J.R. provided unpublished reagents; A.L.S. and E.M.T. performed electron-microscopy-based procedures, and E.M.T. revised the manuscript; M.J.A. conceived experiments, interpreted and analyzed data, and wrote the manuscript.

Funding

This project and B.K. are supported by a project grant awarded by the Fundação para a Ciência e a Tecnologia, Portugal (FCT) [grant number PTDC/IMI-MIC/1142/2012]. S.V.-C. and M.A. are funded by post-doctoral fellowships from FCT [grant numbers SFRH/BPD/94204/2013 and SFRH/BPD/62982/2009, respectively]. M.J.A. is funded by a FCT investigator fellowship [grant number IF/00899/2013]; and E.M.T. and A.L.S. are funded by the Instituto and Fundação Calouste Gulbenkian, Portugal.

Supplementary information

Supplementary information available online at
http://jcs.biologists.org/lookup/suppl/doi:10.1242/jcs.188409/-/DC1

References

Amorim, M. J., Bruce, E. A., Read, E. K. C., Foeglein, A., Mahen, R., Stuart, A. D. and Digard, P. (2011). A Rab11- and microtubule-dependent mechanism for cytoplasmic transport of influenza A virus viral RNA. *J. Virol.* **85**, 4143-4156.

Amorim, M. J., Kao, R. Y. and Digard, P. (2013). Nucleozin targets cytoplasmic trafficking of viral ribonucleoprotein-rab11 complexes in influenza a virus infection. *J. Virol.* **87**, 4694-4703.

Avalos, R. T., Yu, Z. and Nayak, D. P. (1997). Association of influenza virus NP and M1 proteins with cellular cytoskeletal elements in influenza virus-infected cells. *J. Virol.* **71**, 2947-2958.

Avilov, S. V., Moisy, D., Munier, S., Schraidt, O., Naffakh, N. and Cusack, S. (2012a). Replication-competent influenza A virus that encodes a split-green fluorescent protein-tagged PB2 polymerase subunit allows live-cell imaging of the virus life cycle. *J. Virol.* **86**, 1433-1448.

Avilov, S. V., Moisy, D., Naffakh, N. and Cusack, S. (2012b). Influenza A virus progeny vRNP trafficking in live infected cells studied with the virus-encoded fluorescently tagged PB2 protein. *Vaccine* **30**, 7411-7417.

Baetz, N. W. and Goldenring, J. R. (2013). Rab11-family interacting proteins define spatially and temporally distinct regions within the dynamic Rab11a-dependent recycling system. *Mol. Biol. Cell* **24**, 643-658.

Barman, S., Ali, A., Hui, E. K.-W., Adhikary, L. and Nayak, D. P. (2001). Transport of viral proteins to the apical membranes and interaction of matrix protein with glycoproteins in the assembly of influenza viruses. *Virus Res.* **77**, 61-69.

Belov, G. A., Nair, V., Hansen, B. T., Hoyt, F. H., Fischer, E. R. and Ehrenfeld, E. (2012). Complex dynamic development of poliovirus membranous replication complexes. *J. Virol.* **86**, 302-312.

Bergmann, M. and Muster, T. (1995). The relative amount of an influenza A virus segment present in the viral particle is not affected by a reduction in replication of that segment. *J. Gen. Virol.* **76**, 3211-3215.

Bruce, E. A., Medcalf, L., Crump, C. M., Noton, S. L., Stuart, A. D., Wise, H. M., Elton, D., Bowers, K. and Digard, P. (2009). Budding of filamentous and non-filamentous influenza A virus occurs via a VPS4 and VPS28-independent pathway. *Virology* **390**, 268-278.

Chen, B. J., Leser, G. P., Jackson, D. and Lamb, R. A. (2008). The influenza virus M2 protein cytoplasmic tail interacts with the M1 protein and influences virus assembly at the site of virus budding. *J. Virol.* **82**, 10059-10070.

Chou, Y.-Y., Vafabakhsh, R., Doganay, S., Gao, Q., Ha, T. and Palese, P. (2012). One influenza virus particle packages eight unique viral RNAs as shown by FISH analysis. *Proc. Natl. Acad. Sci. USA* **109**, 9101-9106.

Chou, Y.-Y., Heaton, N. S., Gao, Q., Palese, P., Singer, R. and Lionnet, T. (2013). Colocalization of different influenza viral RNA segments in the cytoplasm before viral budding as shown by single-molecule sensitivity FISH analysis. *PLoS Pathog.* **9**, e1003358.

De Wit, E., Spronken, M. I. J., Bestebroer, T. M., Rimmelzwaan, G. F., Osterhaus, A. D. M. E. and Fouchier, R. A. M. (2004). Efficient generation and growth of influenza virus A/PR/8/34 from eight cDNA fragments. *Virus Res.* **103**, 155-161.

Demirov, D., Gabriel, G., Schneider, C., Hohenberg, H. and Ludwig, S. (2012). Interaction of influenza A virus matrix protein with RACK1 is required for virus release. *Cell. Microbiol.* **14**, 774-789.

Eisfeld, A. J., Kawakami, E., Watanabe, T., Neumann, G. and Kawaoka, Y. (2011). RAB11A is essential for transport of the influenza virus genome to the plasma membrane. *J. Virol.* **85**, 6117-6126.

Eisfeld, A. J., Neumann, G. and Kawaoka, Y. (2015). At the centre: influenza A virus ribonucleoproteins. *Nat. Rev. Microbiol.* **13**, 28-41.

Elster, C., Larsen, K., Gagnon, J., Ruigrok, R. W. and Baudin, F. (1997). Influenza virus M1 protein binds to RNA through its nuclear localization signal. *J. Gen. Virol.* **78**, 1589-1596.

Elton, D., Simpson-Holley, M., Archer, K., Medcalf, L., Hallam, R., McCauley, J. and Digard, P. (2001). Interaction of the influenza virus nucleoprotein with the cellular CRM1-mediated nuclear export pathway. *J. Virol.* **75**, 408-419.

Enami, M. and Enami, K. (1996). Influenza virus hemagglutinin and neuraminidase glycoproteins stimulate the membrane association of the matrix protein. *J. Virol.* **70**, 6653-6657.

Fournier, E., Moules, V., Essere, B., Paillart, J.-C., Sirbat, J.-D., Isel, C., Cavalier, A., Rolland, J.-P., Thomas, D., Lina, B. et al. (2012). A supramolecular assembly formed by influenza A virus genomic RNA segments. *Nucleic Acids Res.* **40**, 2197-2209.

Fujii, K., Fujii, Y., Noda, T., Muramoto, Y., Watanabe, T., Takada, A., Goto, H., Horimoto, T. and Kawaoka, Y. (2005). Importance of both the coding and the

segment-specific noncoding regions of the influenza A virus NS segment for its efficient incorporation into virions. *J. Virol.* **79**, 3766-3774.
Gavazzi, C., Isel, C., Fournier, E., Moules, V., Cavalier, A., Thomas, D., Lina, B. and Marquet, R. (2013). An in vitro network of intermolecular interactions between viral RNA segments of an avian H5N2 influenza A virus: comparison with a human H3N2 virus. *Nucleic Acids Res.* **41**, 1241-1254.
Gog, J. R., Afonso, E. D. S., Dalton, R. M., Leclercq, I., Tiley, L., Elton, D., von Kirchbach, J. C., Naffakh, N., Escriou, N. and Digard, P. (2007). Codon conservation in the influenza A virus genome defines RNA packaging signals. *Nucleic Acids Res.* **35**, 1897-1907.
Gorai, T., Goto, H., Noda, T., Watanabe, T., Kozuka-Hata, H., Oyama, M., Takano, R., Neumann, G., Watanabe, S. and Kawaoka, Y. (2012). F1Fo-ATPase, F-type proton-translocating ATPase, at the plasma membrane is critical for efficient influenza virus budding. *Proc. Natl. Acad. Sci. USA* **109**, 4615-4620.
Harak, C. and Lohmann, V. (2015). Ultrastructure of the replication sites of positive-strand RNA viruses. *Virology* **479-480**, 418-433.
Harris, A., Forouhar, F., Qiu, S., Sha, B. and Luo, M. (2001). The crystal structure of the influenza matrix protein M1 at neutral pH: M1-M1 protein interfaces can rotate in the oligomeric structures of M1. *Virology* **289**, 34-44.
He, J., Sun, E., Bujny, M. V., Kim, D., Davidson, M. W. and Zhuang, X. (2013). Dual function of CD81 in influenza virus uncoating and budding. *PLoS Pathog.* **9**, e1003701.
Henriques, R., Griffiths, C., Hesper Rego, E. and Mhlanga, M. M. (2011). PALM and STORM: unlocking live-cell super-resolution. *Biopolymers* **95**, 322-331.
Herfst, S., Imai, M., Kawaoka, Y. and Fouchier, R. A. M. (2014). Avian influenza virus transmission to mammals. *Curr. Top. Microbiol. Immunol.* **385**, 137-155.
Hui, E. K.-W. and Nayak, D. P. (2001). Role of ATP in influenza virus budding. *Virology* **290**, 329-341.
Hui, E. K.-W. and Nayak, D. P. (2002). Role of G protein and protein kinase signalling in influenza virus budding in MDCK cells. *J. Gen. Virol.* **83**, 3055-3066.
Hutchinson, E. C. and Fodor, E. (2013). Transport of the influenza virus genome from nucleus to nucleus. *Viruses* **5**, 2424-2446.
Hutchinson, E. C., Charles, P. D., Hester, S. S., Thomas, B., Trudgian, D., Martínez-Alonso, M. and Fodor, E. (2014). Conserved and host-specific features of influenza virion architecture. *Nat. Commun.* **5**, 4816.
Kao, R. Y., Yang, D., Lau, L.-S., Tsui, W. H. W., Hu, L., Dai, J., Chan, M.-P., Chan, C.-M., Wang, P., Zheng, B.-J. et al. (2010). Identification of influenza A nucleoprotein as an antiviral target. *Nat. Biotechnol.* **28**, 600-605.
Kawaguchi, A., Hirohama, M., Harada, Y., Osari, S. and Nagata, K. (2015). Influenza virus induces cholesterol-enriched endocytic recycling compartments for budozone formation via cell cycle-independent centrosome maturation. *PLoS Pathog.* **11**, e1005284.
Kelly, E. E., Horgan, C. P. and McCaffrey, M. W. (2012). Rab11 proteins in health and disease. *Biochem. Soc. Trans.* **40**, 1360-1367.
Lakadamyali, M., Rust, M. J. and Zhuang, X. (2006). Ligands for clathrin-mediated endocytosis are differentially sorted into distinct populations of early endosomes. *Cell* **124**, 997-1009.
Lakdawala, S. S., Wu, Y., Wawrzusin, P., Kabat, J., Broadbent, A. J., Lamirande, E. W., Fodor, E., Altan-Bonnet, N., Shroff, H. and Subbarao, K. (2014). Influenza a virus assembly intermediates fuse in the cytoplasm. *PLoS Pathog.* **10**, e1003971.
Laliberte, J. P. and Moss, B. (2010). Lipid membranes in poxvirus replication. *Viruses* **2**, 972-986.
Limpens, R. W. A. L., van der Schaar, H. M., Kumar, D., Koster, A. J., Snijder, E. J., van Kuppeveld, F. J. M. and Barcena, M. (2011). The transformation of enterovirus replication structures: a three-dimensional study of single- and double-membrane compartments. *MBio* **2**, e00166-11.
Lindenbach, B. D. and Rice, C. M. (2013). The ins and outs of hepatitis C virus entry and assembly. *Nat. Rev. Microbiol.* **11**, 688-700.
Loussert Fonta, C. and Humbel, B. M. (2015). Correlative microscopy. *Arch. Biochem. Biophys.* **581**, 98-110.
Ma, K., Roy, A.-M. and Whittaker, G. R. (2001). Nuclear export of influenza virus ribonucleoproteins: identification of an export intermediate at the nuclear periphery. *Virology* **282**, 215-220.
Matrosovich, M., Matrosovich, T., Garten, W. and Klenk, H.-D. (2006). New low-viscosity overlay medium for viral plaque assays. *Virol. J.* **3**, 63.
McCown, M. F. and Pekosz, A. (2006). Distinct domains of the influenza a virus M2 protein cytoplasmic tail mediate binding to the M1 protein and facilitate infectious virus production. *J. Virol.* **80**, 8178-8189.
McGeoch, D., Fellner, P. and Newton, C. (1976). Influenza virus genome consists of eight distinct RNA species. *Proc. Natl. Acad. Sci. USA* **73**, 3045-3049.
Mobius, W., van Donselaar, E., Ohno-Iwashita, Y., Shimada, Y., Heijnen, H. F. G., Slot, J. W. and Geuze, H. J. (2003). Recycling compartments and the internal vesicles of multivesicular bodies harbor most of the cholesterol found in the endocytic pathway. *Traffic* **4**, 222-231.
Momose, F., Kikuchi, Y., Komase, K. and Morikawa, Y. (2007). Visualization of microtubule-mediated transport of influenza viral progeny ribonucleoprotein. *Microbes Infect.* **9**, 1422-1433.
Momose, F., Sekimoto, T., Ohkura, T., Jo, S., Kawaguchi, A., Nagata, K. and Morikawa, Y. (2011). Apical Transport of influenza A virus ribonucleoprotein requires Rab11-positive recycling endosome. *PLoS ONE* **6**, e21123.
Monaghan, P., Cook, H., Jackson, T., Ryan, M. and Wileman, T. (2004). The ultrastructure of the developing replication site in foot-and-mouth disease virus-infected BHK-38 cells. *J. Gen. Virol.* **85**, 933-946.
Morens, D. M., Taubenberger, J. K. and Fauci, A. S. (2009). The persistent legacy of the 1918 influenza virus. *N. Engl. J. Med.* **361**, 225-229.
Noda, T., Sagara, H., Yen, A., Takada, A., Kida, H., Cheng, R. H. and Kawaoka, Y. (2006). Architecture of ribonucleoprotein complexes in influenza A virus particles. *Nature* **439**, 490-492.
Noton, S. L., Medcalf, E., Fisher, D., Mullin, A. E., Elton, D. and Digard, P. (2007). Identification of the domains of the influenza A virus M1 matrix protein required for NP binding, oligomerization and incorporation into virions. *J. Gen. Virol.* **88**, 2280-2290.
Rink, J., Ghigo, E., Kalaidzidis, Y. and Zerial, M. (2005). Rab conversion as a mechanism of progression from early to late endosomes. *Cell* **122**, 735-749.
Sato, M., Grant, B. D., Harada, A. and Sato, K. (2008). Rab11 is required for synchronous secretion of chondroitin proteoglycans after fertilization in Caenorhabditis elegans. *J. Cell Sci.* **121**, 3177-3186.
Schonteich, E., Wilson, G. M., Burden, J., Hopkins, C. R., Anderson, K., Goldenring, J. R. and Prekeris, R. (2008). The Rip11/Rab11-FIP5 and kinesin II complex regulates endocytic protein recycling. *J. Cell Sci.* **121**, 3824-3833.
Shaw, M. L., Stone, K. L., Colangelo, C. M., Gulcicek, E. E. and Palese, P. (2008). Cellular proteins in influenza virus particles. *PLoS Pathog.* **4**, e1000085.
Simpson-Holley, M., Ellis, D., Fisher, D., Elton, D., McCauley, J. and Digard, P. (2002). A functional link between the actin cytoskeleton and lipid rafts during budding of filamentous influenza virions. *Virology* **301**, 212-225.
Stenmark, H., Parton, R. G., Steele-Mortimer, O., Lutcke, A., Gruenberg, J. and Zerial, M. (1994). Inhibition of rab5 GTPase activity stimulates membrane fusion in endocytosis. *EMBO J.* **13**, 1287-1296.
Stone, R., Hayashi, T., Bajimaya, S., Hodges, E. and Takimoto, T. (2015). Critical role of Rab11a-mediated recycling endosomes in the assembly of type I parainfluenza viruses. *Virology* **487**, 11-18.
Sugita, Y., Sagara, H., Noda, T. and Kawaoka, Y. (2013). Configuration of viral ribonucleoprotein complexes within the influenza A virion. *J. Virol.* **87**, 12879-12884.
Wei, J., Liu, Y., Bose, K., Henry, G. D. and Baleja, J. D. (2009). Disorder and structure in the Rab11 binding domain of Rab11 family interacting protein 2. *Biochemistry* **48**, 549-557.
Welsch, S., Miller, S., Romero-Brey, I., Merz, A., Bleck, C. K. E., Walther, P., Fuller, S. D., Antony, C., Krijnse-Locker, J. and Bartenschlager, R. (2009). Composition and three-dimensional architecture of the dengue virus replication and assembly sites. *Cell Host Microbe* **5**, 365-375.
Welz, T., Wellbourne-Wood, J. and Kerkhoff, E. (2014). Orchestration of cell surface proteins by Rab11. *Trends Cell Biol.* **24**, 407-415.
Xiong, B., Bayat, V., Jaiswal, M., Zhang, K., Sandoval, H., Charng, W.-L., Li, T., David, G., Duraine, L., Lin, Y.-Q. et al. (2012). Crag is a GEF for Rab11 required for rhodopsin trafficking and maintenance of adult photoreceptor cells. *PLoS Biol.* **10**, e1001438.
Yamayoshi, S., Watanabe, M., Goto, H. and Kawaoka, Y. (2015). Identification of A novel viral protein expressed from the PB2 segment of influenza A Virus. *J. Virol.* **90**, 444-456.
Ye, Z., Liu, T., Offringa, D. P., Mcinnis, J. and Levandowski, R. A. (1999). Association of influenza virus matrix protein with ribonucleoproteins. *J. Virol.* **73**, 7467-7473.
Zhang, X.-M., Ellis, S., Sriratana, A., Mitchell, C. A. and Rowe, T. (2004). Sec15 is an effector for the Rab11 GTPase in mammalian cells. *J. Biol. Chem.* **279**, 43027-43034.
Zhang, K., Wang, Z., Fan, G.-Z., Wang, J., Gao, S., Li, Y., Sun, L., Yin, C.-C. and Liu, W.-J. (2015). Two polar residues within C-terminal domain of M1 are critical for the formation of influenza A Virions. *Cell Microbiol.* **17**, 1583-1593.
Zhao, H., Ekstrom, M. and Garoff, H. (1998). The M1 and NP proteins of influenza A virus form homo- but not heterooligomeric complexes when coexpressed in BHK-21 cells. *J. Gen. Virol.* **79**, 2435-2446.

Journal of Cell Science

Supplementary Figures

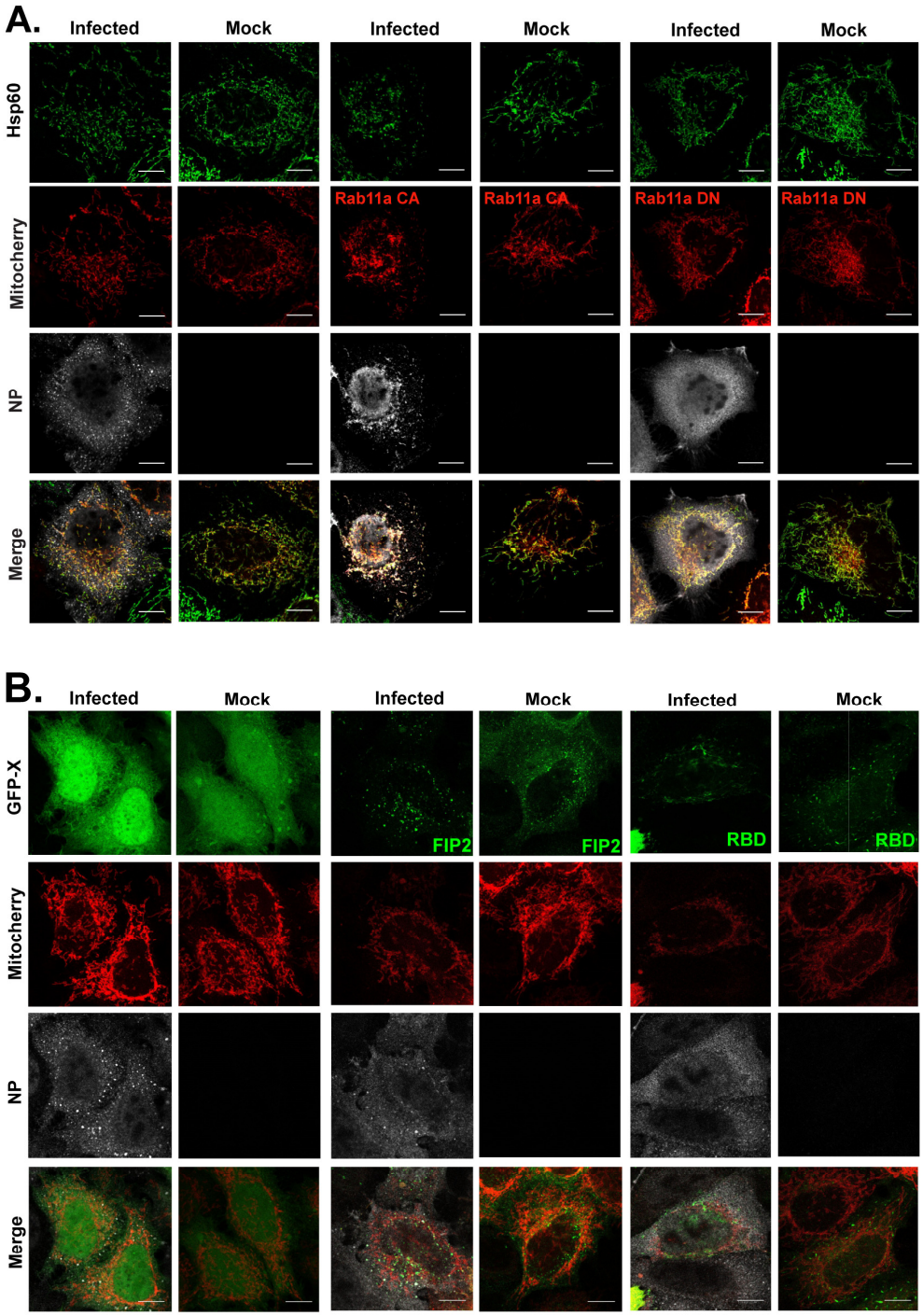

Journal of Cell Science • Supplementary information

Figure S1 - FIPs and vRNPs compete for direct binding to mitoRab11a CA, but not mitoRab11a DN or mitocherry.

A. CA and DN forms of Rab11a protein tagged with cherry at the N-terminus, or cherry only, were targeted to the mitochondria by fusion with the mitochondrial targeting sequence (MTS) of Tom20 (=mitoRab11a CA / mitoRab11 DN / mitocherry). HeLa cells were transfected with these three plasmids individually and infected with PR8 at MOI 20. At 14h p.i., cells were fixed and processed for immunofluorescence staining of Hsp60 and/or viral NP. **B.** HeLa cells were co-transfected with mitocherry and either GFP alone (X=-) or GFP-X (X=FIPs) and sequentially infected or mock-infected with PR8 at MOI 20. At 14h p.i., cells were fixed and processed for immunofluorescence staining of viral NP. Bar=10 μm. Images are representative of two independent experiments. An average of 30 cells was analyzed per condition per experiment.

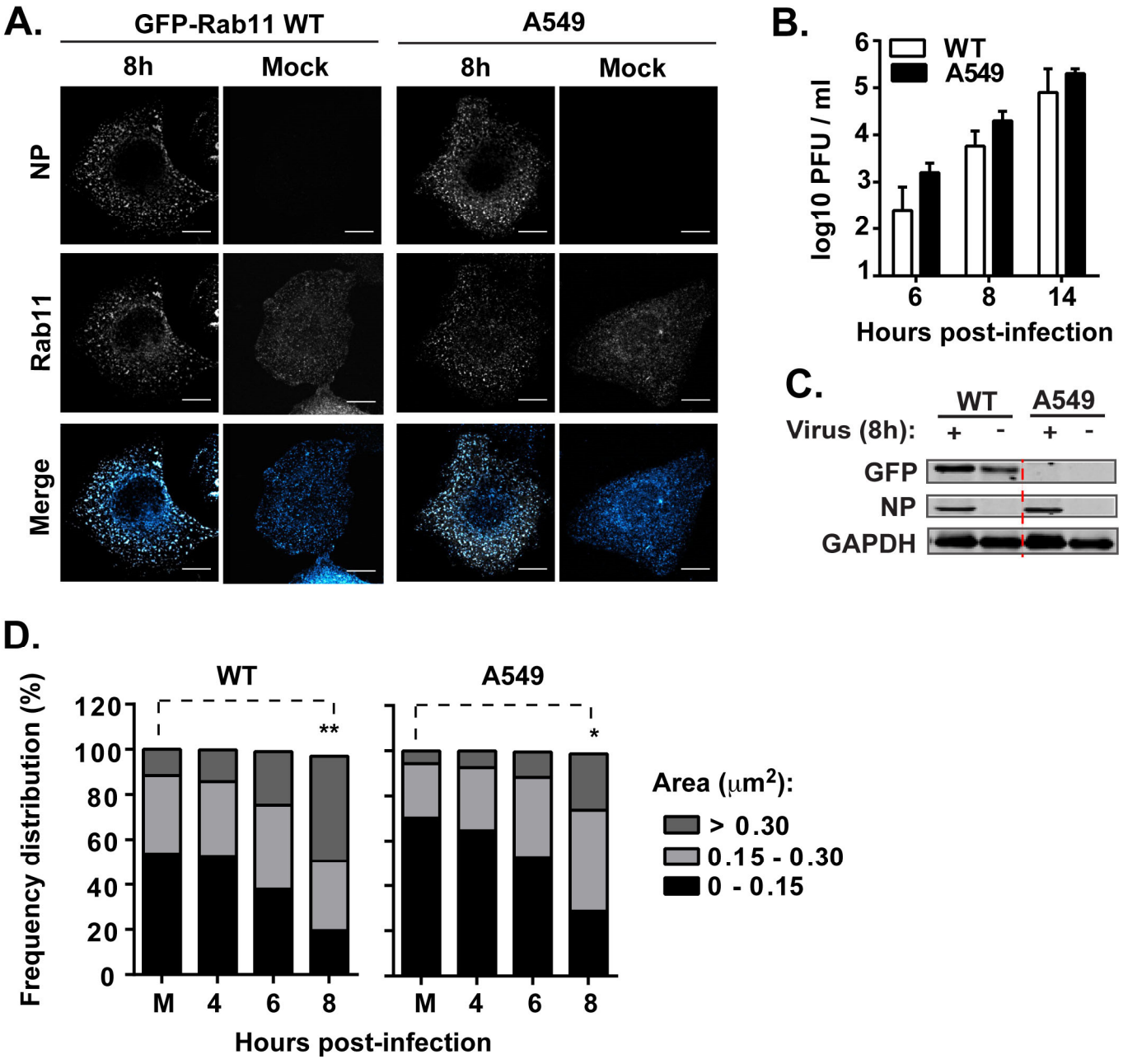

Figure S2 - Cells stably overexpressing GFP-Rab11a behave similarly to cells expressing endogenous levels of Rab11a.

A549 cells alone or stably overexpressing GFP-Rab11a WT were infected or mock (M)-infected with PR8 at MOI 3. At the indicated time points: **A.** Cells were fixed and processed for immunofluorescence staining of Rab11 and viral NP. Bar=10 μm. **B.** Viral titres were quantified by

plaque formation on MDCK cells and expressed as the logarithm 10 of plaque forming units (PFU) per ml ± SEM. Statistical analysis of data was performed using two-way ANOVA, followed by a Dunnett's multiple comparisons test (no significant differences detected). **C.** GFP-tagged proteins, viral NP and GAPDH levels were detected by Western blot. **D.** The frequency distributions (%) of small, medium and large Rab11-vesicle areas (μm^2) were plotted over the course of infection. Statistical analysis of data was performed using a two-way ANOVA test, followed by Tukey's multiple comparisons test (*$p<0.05$; **$p<0.01$). Experiments were performed twice and an average of 30 cells per experiment were analysed.

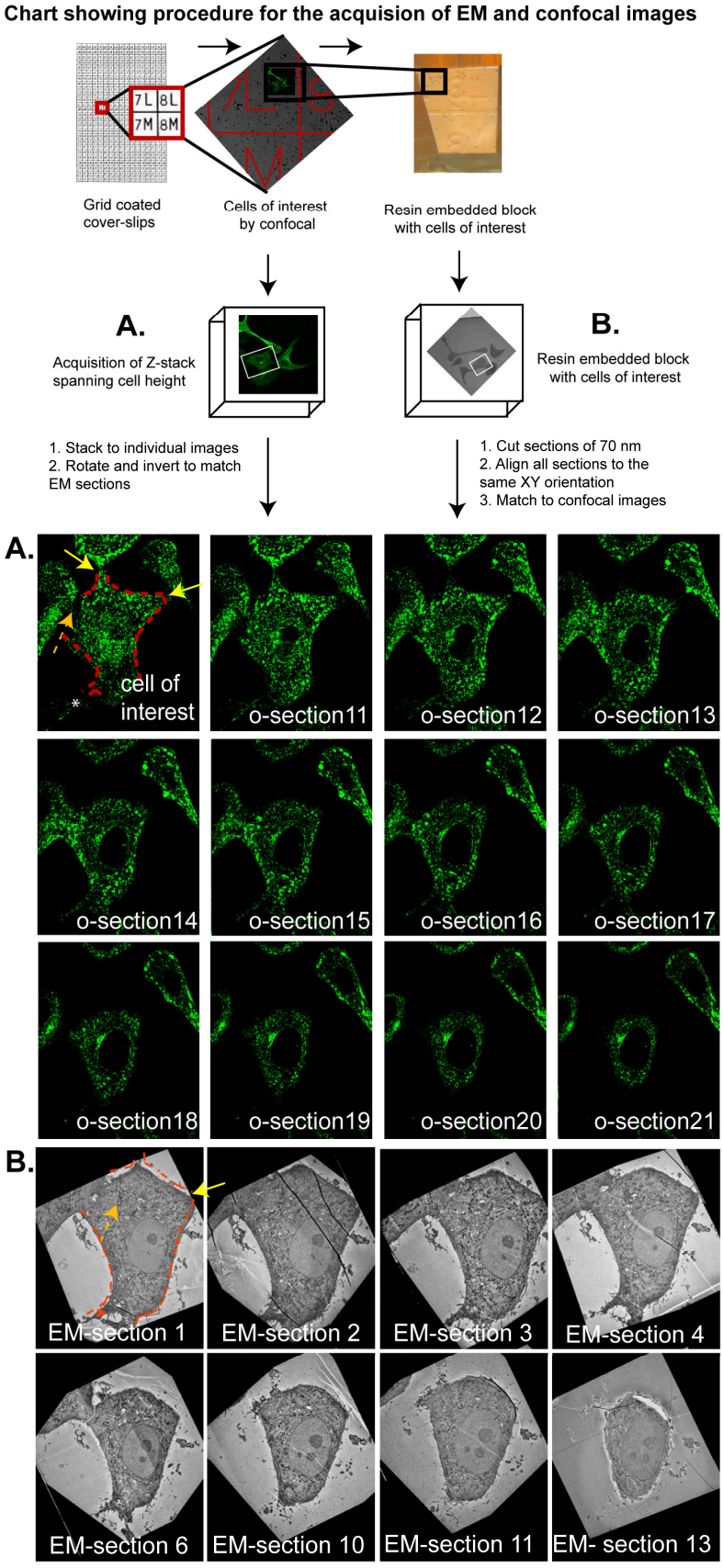

Figure S3 - Strategy to acquire images of cells of interest by confocal and electron microscopy images.

A549 cells stably expressing GFP-Rab11a were grown on gridded coverslips, infected with PR8 at a MOI of 3. **A.** Cells were fixed and imaged for confocal microscopy to acquire Z-stacks of the cells of interest. **B.** Cells were then processed for electron microscopy (EM), serial sectioned at 70 nm and imaged using the electron microscope, throughout the whole depth of the cell. **A. B.** Images spanning the entire volume of the cell from confocal (o-section) and EM (EM-section) were observed to make correspondence between the two methods. Cell shape, cell-to-cell contacts (see arrows) and cell holes (see asterisk in the first confocal image and EM section 1) were taken into consideration to match confocal and EM serial sections.

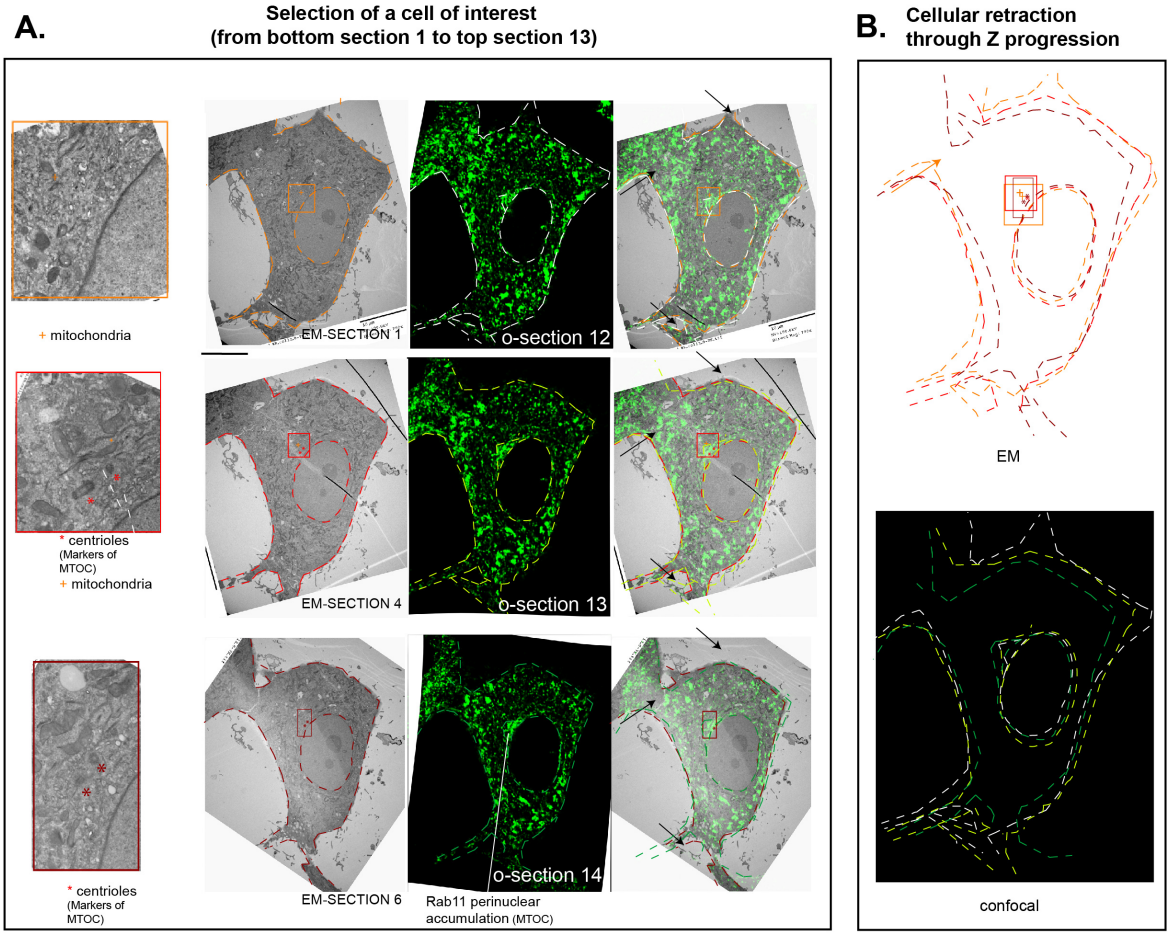

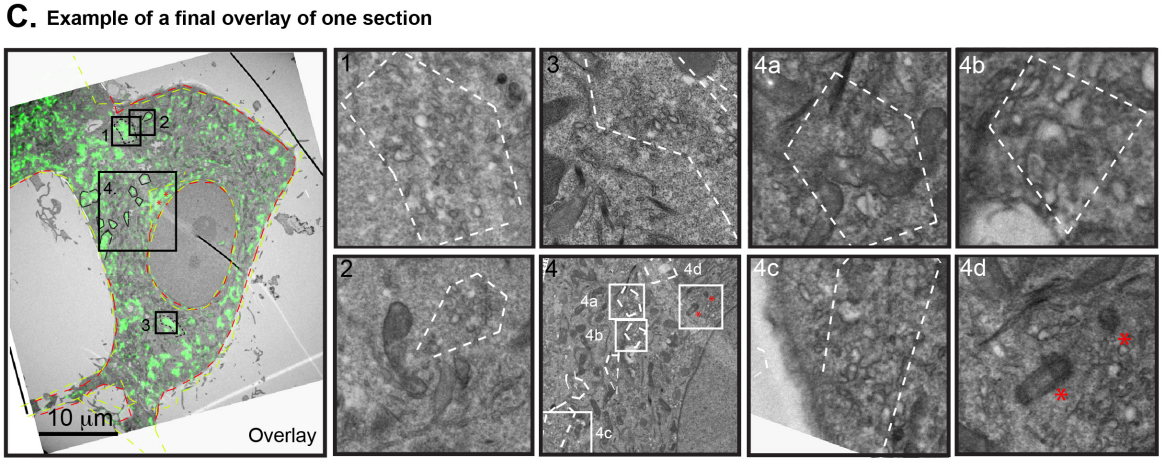

Figure S4 - Strategy to refine alignment between confocal and EM images.

A. Matching between confocal and EM images was refined using structural features that include: cell-to-cell contacts (arrows) that are established or lost when moving away the basal side; centrioles as markers of the microtubule organizing center (MTOC) in EM and Rab11 accumulation

in the same region by confocal; nuclei size, cell holes (see asterisk in the first confocal image and EM section 1). **B.** Parameters evaluated to confirm alignment included cell shape variation during Z-stack progression by EM (top) and confocal imaging (bottom) between serial sections. **C.** Example of a final figure containing ultrastructural details from the Overlay image. The Overlay image corresponds to a section in the confocal and EM matched as explained in Figure S6 and S7A. The detailed regions were obtained by delineating the green areas in the Overlay with dashed lines, and drawing a square around the area to be magnified. These marks were amplified to fit the edges of EM figures of higher magnification without any distortions. The process was repeated to further amplify areas of interest that resulted in series 4a-d. Features like the MTOC, easily detected in both systems validated the alignment. For this, we used the described Rab11 accumulation at the perinuclear region surrounding the MTOC observable by confocal to successfully predict the location of the centrioles in EM images (red asterisks in 4d).